SSWD-EvoEpi: A Coupled Eco-Evolutionary Epidemiological Model for Sea Star Wasting Disease in *Pycnopodia helianthoides*

Technical Report — Model Development and Sensitivity Analysis

Willem Weertman[1,2]

[1]Department of Psychology, University of Washington, Seattle, WA

[2]Friday Harbor Laboratories, University of Washington, Friday Harbor, WA

February 21, 2026

Abstract

Sea star wasting disease (SSWD) caused one of the largest wildlife mass mortality events in marine ecosystems, driving the sunflower sea star (*Pycnopodia helianthoides*) to a 90.6% range-wide decline and IUCN Critically Endangered status. The recent identification of *Vibrio pectenicida* strain FHCF-3 as a causative agent, combined with active captive breeding and the first experimental outplanting of captive-bred juveniles, creates an urgent need for quantitative tools to guide recovery. We present SSWD-EvoEpi, an individual-based, spatially explicit eco-evolutionary epidemiological model coupling *V. pectenicida* transmission dynamics with polygenic host evolution under sweepstakes reproductive success. Each agent carries a diploid genotype across 51 loci governing three fitness-related traits — resistance (immune exclusion), tolerance (damage limitation), and recovery (pathogen clearance) — that evolve in response to disease-driven selection. Disease dynamics follow an SEIR compartmental structure with an environmental pathogen reservoir, pathogen evolution along a virulence–transmission tradeoff, and temperature-dependent forcing. Reproduction implements sweepstakes reproductive success with $N_e/N \sim 10^{-3}$, sex-asymmetric spawning induction, and post-spawning immunosuppression. Four rounds of global sensitivity analysis (Morris screening and Sobol variance decomposition) across up to 47 parameters reveal that model behavior is dominated by nonlinear interactions among disease mortality rate, host susceptibility, environmental pathogen pressure, and genetic architecture, with recovery

1

trait evolution emerging as the fastest adaptive response. The model provides a framework for evaluating captive-bred release strategies, assisted gene flow, and the feasibility of evolutionary rescue on conservation-relevant timescales.

Contents

1 Introduction

1.1 Sea Star Wasting Disease and the Collapse of *Pycnopodia helianthoides*

Sea star wasting disease (SSWD) caused one of the largest documented wildlife mass mortality events in marine ecosystems when it swept through populations of over 20 asteroid species along the northeastern Pacific coast beginning in 2013 [23, 29, 47]. The disease, characterized by behavioral changes (arm twisting, lethargy), loss of turgor, body wall lesions, ray autotomy, and rapid tissue degradation, devastated populations from Baja California to the Gulf of Alaska within months [32, 46]. Among the species affected, the sunflower sea star (*Pycnopodia helianthoides*) suffered the most catastrophic decline, losing an estimated 5.75 billion individuals and experiencing a 90.6% range-wide population reduction based on 61,043 surveys across 31 datasets [19, 24]. Along the outer coast from Washington to Baja California, declines exceeded 97%, with many regions recording zero individuals in subsequent surveys [19, 22]. The species was assessed as Critically Endangered by the IUCN in 2021 [19] and is under consideration for listing as Threatened under the U.S. Endangered Species Act [39].

As a large-bodied, mobile, generalist predator capable of consuming sea urchins at rates sufficient to structure entire subtidal communities, *Pycnopodia helianthoides* functions as a keystone species in northeastern Pacific kelp forest ecosystems [6, 15, 44]. Its precipitous decline has been linked to cascading trophic effects, including sea urchin population explosions and extensive kelp forest deforestation, with northern California losing 96% of its kelp canopy since the 2014 marine heatwave [45, 51]. The loss of this apex predator thus represents not only a conservation crisis for a single species but a destabilization of an entire marine ecosystem [22, 36].

1.2 Etiology: A Decade-Long Mystery Resolved

For over a decade following the initial outbreak, the causative agent of SSWD remained contested. An early hypothesis implicating sea star associated densovirus (SSaDV; Hewson et al. 29) was subsequently retracted after repeated failures to reproduce the original challenge experiments and the discovery that the virus is endemic in healthy echinoderm populations worldwide [30–32]. An alternative hypothesis invoking boundary layer oxygen depletion (BLODL) at the animal–water interface proposed that microbial respiration on sea star surfaces draws down dissolved oxygen, leading to tissue hypoxia [2, 27]. While this mechanism may contribute to disease susceptibility, it did not identify a specific pathogen.

The breakthrough came with Prentice et al. [49], who fulfilled Koch's postulates by demonstrating that *Vibrio pectenicida* strain FHCF-3, a Gram-negative marine bac-

terium, is a causative agent of SSWD in *Pycnopodia helianthoides*. Through seven controlled exposure experiments using captive-bred, quarantined sea stars, the authors showed that injection of cultured *V. pectenicida* FHCF-3 into the coelomic cavity reliably produced disease signs — arm twisting, lesion formation, autotomy, and death within approximately two weeks. Heat-treated and 0.22 μm filtered controls remained healthy, confirming a living bacterial agent. Critically, the pathogen was re-isolated from experimentally infected animals, completing Koch's postulates. Earlier investigations had missed *V. pectenicida* because they sampled body wall tissue rather than coelomic fluid, where the bacterium resides.

However, the etiological picture is not entirely resolved. Hewson [28] demonstrated that *V. pectenicida* FHCF-3 was not consistently detected in non-*Pycnopodia helianthoides* species during the 2013–2014 mass mortality, suggesting it may be specific to *Pycnopodia helianthoides* or may function as an opportunistic pathogen rather than a universal SSWD agent across all affected asteroid taxa. The bacterium also exhibits explosive growth in the presence of decaying echinoderm tissue, raising questions about whether it acts primarily as a pathogen or a saprobe under different conditions [28]. Nonetheless, for *Pycnopodia helianthoides* — the focus of this study — the evidence for *V. pectenicida* as the primary causative agent is robust. The identification of a specific bacterial pathogen with known temperature-dependent growth dynamics [42] provides a mechanistic basis for modeling disease transmission and environmental forcing.

1.3 Conservation Urgency and Active Recovery Efforts

The failure of *Pycnopodia helianthoides* populations to recover naturally in the decade following the initial epizootic — contrasting with partial recovery observed in some co-occurring asteroid species [18] — has motivated intensive conservation action. The species' long generation time (∼30 years), broadcast spawning reproductive strategy, and vulnerability to Allee effects at low density [16, 40] compound the challenge of natural recovery. Historical precedent is sobering: the Caribbean long-spined sea urchin *Diadema antillarum*, which suffered a comparable 93–100% mass mortality in 1983–1984, achieved only ∼12% recovery after three decades [37]. Another asteroid, *Heliaster kubiniji*, has never recovered from a 1975 mass mortality event in the Gulf of California [12].

In response, a coordinated multi-partner recovery effort has emerged. The Association of Zoos and Aquariums (AZA) Saving Animals From Extinction (SAFE) program maintains over 2,500 captive juveniles and 130+ reproductive adults across 17 AZA institutions [5]. The first experimental outplanting of captive-bred *Pycnopodia helianthoides* occurred in December 2025 in Monterey, California, with 47 of 48 juveniles surviving after four weeks [59]. A Roadmap to Recovery developed by over 30 leading experts defines regionally nested recovery objectives, from local demographic benchmarks to range-wide

genetic structure targets [24]. Cryopreservation of gametes has been demonstrated for a congener and is under development for *Pycnopodia helianthoides* to enable assisted gene flow from genetically diverse founders [21, 57]. In 2025, the California Ocean Protection Council approved $630,000 in funding for captive breeding, disease diagnostics, and experimental outplanting [7]. A reference genome has also been published [56], laying the groundwork for genome-wide association studies (GWAS) to identify resistance loci.

These recovery efforts require quantitative predictions: How many captive-bred individuals should be released, where, and when? What are the genetic consequences of releasing animals from a limited captive founder population? Can natural selection drive resistance evolution fast enough to matter on conservation timescales? How do pathogen evolution, environmental change, and spatial structure interact to shape recovery trajectories? Answering these questions demands a modeling framework that integrates disease dynamics with population genetics in an explicitly spatial context.

1.4 The Need for an Eco-Evolutionary Framework

Existing models of SSWD dynamics have focused on either epidemiological or ecological aspects in isolation. Aalto et al. [1] coupled an SIR-type model with ocean circulation to explain the rapid continental-scale spread of SSWD, finding that temperature-dependent mortality best matched observed patterns. Tolimieri [60] conducted a population viability analysis using stage-structured matrix models but did not incorporate disease dynamics or host genetics. Arroyo-Esquivel et al. [4] recently modeled epidemiological consequences of managed reintroduction following disease-driven host decline, but their framework lacks genetic evolution. None of these approaches captures the interplay between disease-driven selection, host genetic adaptation, and demographic recovery that is central to predicting conservation outcomes.

The theoretical motivation for coupling these processes is compelling. Mass mortality events impose intense directional selection on host populations [54], and in *Pisaster ochraceus* — a co-occurring sea star affected by SSWD — rapid allele frequency shifts ($\Delta q \approx 0.08$–0.15 at outlier loci) were detected within a single generation of the epizootic, with geographic consistency across sites indicating selection rather than drift [54]. However, in broadcast-spawning marine invertebrates, the genetic consequences of mass mortality are filtered through sweepstakes reproductive success (SRS), whereby variance in individual reproductive success is so large that effective population size (N_e) is orders of magnitude smaller than census size ($N_e/N \sim 10^{-3}$; Árnason et al. 3, Hedgecock and Pudovkin 25). SRS amplifies genetic drift on ecological timescales [61], can facilitate rapid adaptation when coupled with bottlenecks [14], and generates chaotic genetic patchiness that confounds simple predictions of evolutionary trajectories. Any model of evolutionary rescue in *Pycnopodia helianthoides* must therefore account for this fundamental feature

8

of marine broadcast spawner genetics.

The closest methodological precedent is the eco-evolutionary individual-based model (IBM) developed by Clement et al. [10] for coevolution between Tasmanian devils (*Sarcophilus harrisii*) and devil facial tumour disease (DFTD). That model coupled an SEI epidemiological framework with polygenic quantitative genetics, parameterized from two decades of field data and GWAS results, and found a high probability of host persistence over 50 generations through coevolutionary dynamics. Our model extends this approach to a marine system with fundamentally different reproductive biology — broadcast spawning with sweepstakes reproductive success, external fertilization subject to Allee effects, and a pelagic larval phase mediating spatial connectivity — challenges that no existing eco-evolutionary disease model has addressed.

1.5 Model Overview

We present SSWD-EvoEpi, an individual-based, spatially explicit, eco-evolutionary epidemiological model designed to simulate SSWD dynamics and evolutionary responses in *Pycnopodia helianthoides* metapopulations across the northeastern Pacific. The model tracks individual sea stars as agents within a network of habitat nodes connected by larval dispersal and pathogen transport. Each agent carries a diploid genotype across 51 loci governing three fitness-related traits: resistance (r_i, 17 loci; immune exclusion reducing infection probability), tolerance (t_i, 17 loci; damage limitation extending survival during late-stage infection), and recovery (c_i, 17 loci; pathogen clearance enabling transition from infected to recovered states). Per-locus allele frequencies are drawn from a Beta(2,8) distribution, reflecting polygenic architecture with most loci at low frequency [34].

Disease dynamics follow an SEIR-type compartmental structure with exposed (E), early infected (I_1), and late infected (I_2) stages, coupled with an environmental pathogen reservoir (P) whose dynamics are temperature-dependent [17, 42]. Pathogen evolution is modeled through a heritable virulence phenotype that evolves along a mechanistic tradeoff curve linking shedding rate to host survival duration. Reproduction incorporates sweepstakes reproductive success via a heavy-tailed offspring distribution producing N_e/N ratios consistent with empirical estimates for marine broadcast spawners [25], with sex-asymmetric spawning induction and post-spawning immunosuppression derived from species-specific observations. Spatial connectivity is implemented through distinct larval exchange and pathogen dispersal matrices computed from overwater distances across the model domain.

The model is implemented in Python with NumPy-vectorized agent operations, achieving sufficient performance for large-scale sensitivity analysis and calibration (75,000 agents across 150 nodes in $\sim$72 s). Four rounds of sensitivity analysis using Morris screening and Sobol variance decomposition across up to 47 parameters have identified the key drivers of

9

model behavior, revealing strong nonlinear interactions and highlighting priority targets for empirical calibration.

1.6   Paper Outline

The remainder of this paper is organized as follows. Section 2 describes the overall model architecture, agent representation, and simulation flow. Sections 3–6 detail the disease, genetics, population dynamics, and spatial modules, respectively. Section 7 presents four rounds of global sensitivity analysis, identifying the parameters with greatest influence on epidemiological, demographic, and evolutionary outcomes. Section 8 describes model validation against available empirical data. Section 9 synthesizes findings, discusses limitations, and outlines the path toward calibrated conservation scenario evaluation. Parameter tables and supplementary analyses are provided in Appendix A.

2   Model Architecture

SSWD-EvoEpi is an individual-based model (IBM) that couples epidemiological, demographic, genetic, and spatial dynamics to simulate the eco-evolutionary consequences of sea star wasting disease in *Pycnopodia helianthoides*. Each agent represents a single sea star tracked through its complete life history, carrying a diploid genotype at 51 loci that determines three quantitative defense traits against *Vibrio pectenicida*. We chose an individual-based approach over compartmental (ODE/PDE) models because SSWD dynamics depend critically on individual-level heterogeneity in genetic resistance, body size, spatial position, and disease stage—features that compartmental models cannot represent without substantial loss of biological realism [11, 20].

2.1   Agent Representation

Each individual is represented as a record in a NumPy structured array (`AGENT_DTYPE`) comprising approximately 59 bytes per agent. Table 1 summarizes the principal state variables grouped by functional module.

Table 1: Agent state variables in SSWD-EvoEpi.

Module	Field	Description
Spatial	x, y	Position within node habitat (m)
	heading	Movement heading (rad)
	speed	Instantaneous speed (m min^{-1})
	node_id	Home node index
Life history	size	Arm-tip diameter (mm)
	age	Age (years, fractional)
	stage	Life stage (0–4; Table 2)
	sex	Sex (0 = female, 1 = male)
Disease	disease_state	Compartment (S/E/I$_1$/I$_2$/D/R)
	disease_timer	Days remaining in current disease stage
Genetics	resistance	Resistance score $r_i \in [0,1]$
	tolerance	Tolerance score $t_i \in [0,1]$
	recovery_ability	Recovery/clearance score $c_i \in [0,1]$
Spawning	has_spawned	Bout count this season
	immunosuppression_timer	Post-spawning immunosuppression (days)
Administrative	alive	Active flag
	origin	Wild / captive-bred / AGF / wild-source
	pathogen_virulence	Virulence of infecting strain v_i

Genotypes are stored in a separate array of shape $(N_{\max}, 51, 2)$ with int8 entries, where axis 1 indexes loci and axis 2 indexes the two allele copies (diploid). This separation from the agent record improves cache performance during non-genetic operations (disease transmission, movement), which need not touch the genotype array.

Table 2: Life stages and size thresholds for *Pycnopodia helianthoides*.

Index	Stage	Size threshold (mm)	Reproductive
0	Egg/Larva	—	No
1	Settler	Settlement	No
2	Juvenile	≥ 10	No
3	Subadult	≥ 150	No
4	Adult	≥ 400	Yes

2.2 Node Structure

The spatial domain is represented as a metapopulation network of K discrete habitat nodes. Each node encapsulates:

- A population of agents (structured array + genotype array), initialized at local carrying capacity;

- Environmental state: sea surface temperature $T(t)$ (sinusoidal annual cycle with warming trend), salinity S, and tidal flushing rate ϕ_k;

- A local Vibrio concentration $P_k(t)$ (bacteria mL^{-1});

- Node metadata: latitude, habitat area, fjord classification.

Inter-node coupling occurs through two connectivity matrices:

1. **Pathogen dispersal matrix D**: governs daily exchange of waterborne *Vibrio pectenicida* between nodes, parameterized with an exponential distance kernel (scale $D_P = 15\,\mathrm{km}$);

2. **Larval connectivity matrix C**: governs annual dispersal of competent larvae among nodes, parameterized with a broader kernel (scale $D_L = 400\,\mathrm{km}$) reflecting the extended pelagic larval duration of *Pycnopodia helianthoides*.

2.3 Simulation Loop

The simulation advances in daily timesteps ($\Delta t = 1\,\mathrm{day}$) nested within an annual cycle. At each daily step, the following operations are executed in sequence at every node (Figure **??**):

1. **Environment update.** Compute $T_k(t)$ from a sinusoidal annual SST function with linear warming trend; update flushing rate ϕ_k (seasonally modulated for fjord nodes); salinity is constant per node.

2. **Movement.** Agents execute a correlated random walk (CRW) with 24 hourly substeps per day. Movement speed is modulated by disease state ($\times 0.5$ for I_1, $\times 0.1$ for I_2, $\times 0$ for D). Elastic boundary reflection constrains agents within the habitat.

3. **Disease dynamics.** Vibrio concentration is updated via an Euler step of the pathogen ODE. Susceptible agents are exposed to a force of infection that depends on local pathogen density, individual resistance, salinity, and body size. Infected agents progress through the SEIPD+R compartments with Erlang-distributed stage durations (Section 3).

4. **Pathogen dispersal.** Vibrio is exchanged between neighboring nodes via the **D** matrix, representing waterborne transport.

5. **Settlement.** Larval cohorts whose pelagic larval duration (PLD) has elapsed are settled into the local population via Beverton–Holt density-dependent recruitment, modulated by an adult-presence settlement cue (Allee effect).

6. **Spawning.** During the spawning season (November–July), reproductively mature adults spawn stochastically with daily probability modulated by a seasonal Gaussian envelope centered on the peak spawning day. Female and male multi-bout spawning, sex-asymmetric cascade induction, and post-spawning immunosuppression are modeled explicitly.

7. **Daily demographics.** Natural mortality is applied as a daily probability converted from stage-specific annual survival rates:

$$p_{\text{death,daily}} = 1 - S_{\text{annual}}^{1/365}, \tag{1}$$

with a senescence overlay for individuals exceeding the senescence age ($\tau_{\text{sen}} = 50\,\text{yr}$). Growth follows the von Bertalanffy differential form with daily-scaled stochastic noise; stage transitions are one-directional based on size thresholds (Table 2).

At the end of each simulated year, an annual step performs:

1. **Larval dispersal** via the connectivity matrix **C**: unsettled cohorts from all nodes are pooled, redistributed probabilistically among destination nodes, and settled at receiving nodes or retained in a pending queue for next-year daily settlement.

2. **Disease introduction** (at the designated epidemic year): a fixed number of agents per node are seeded in the Exposed (E) compartment.

3. **Genetic recording**: per-node allele frequencies, additive genetic variance V_A, and trait means are logged annually. Pre- and post-epidemic allele frequency snapshots are captured for calibration against genomic data.

2.4 Design Rationale

Several design choices distinguish SSWD-EvoEpi from previous SSWD models:

Individual-based representation. SSWD mortality is strongly size-dependent [OR = 1.23 per 10 mm; 13], genetically mediated [55], and spatially heterogeneous. A compartmental SIR/SEIR model would require aggregating these axes of variation into homogeneous classes, losing the emergent eco-evolutionary dynamics that arise from individual

13

heterogeneity in resistance, tolerance, and recovery. Following Clement et al. [9], who demonstrated that individual-based eco-evolutionary models are essential for predicting host–pathogen coevolution in Tasmanian devil facial tumor disease, we track each individual's genotype, phenotype, and infection history explicitly.

Continuous daily demographics. Rather than applying mortality, growth, and reproduction as annual pulses, SSWD-EvoEpi evaluates natural mortality and growth daily (Eq. 1), with spawning resolved to individual daily events across a multi-month season. This avoids artificial synchronization artifacts and allows disease–demography interactions (e.g., post-spawning immunosuppression) to operate on their natural timescales.

Separated genotype storage. The 51-locus diploid genotype array (102 bytes per agent) is stored separately from the agent state record. This ensures that the most frequently accessed fields during daily disease and movement updates (position, disease state, size) occupy contiguous memory, improving CPU cache performance by a factor of $\sim$2–3$\times$ in profiled benchmarks.

Three-trait genetic architecture. The 51 loci are partitioned into three independently segregating trait blocks of 17 loci each, controlling resistance (immune exclusion), tolerance (damage limitation), and recovery (pathogen clearance). This architecture captures the empirical observation that host defense against infectious disease operates through mechanistically distinct pathways that can evolve semi-independently [50].

3 Disease Module

The disease module implements a stochastic, environmentally driven SEIPD+R (Susceptible–Exposed–Infectious$_1$–Infectious$_2$–Dead, plus Recovered) compartmental framework operating at the individual level. Each agent carries its own disease state, countdown timer, genetic defense traits (r_i, t_i, c_i), and (when pathogen evolution is enabled) the virulence phenotype v_i of its infecting strain. Disease dynamics are resolved daily at each spatial node, coupled to the environmental forcing module for temperature-dependent rates and to the genetics module for individual susceptibility.

3.1 Compartmental Structure

The disease pathway consists of five compartments plus a recovery state (Figure **??**):

- **S (Susceptible):** Healthy, at risk of infection.

- **E (Exposed):** Latently infected; not yet shedding pathogen. Duration is Erlang-distributed with shape $k_E = 3$.

- **I_1 (Early infectious):** Pre-symptomatic shedding at rate $\sigma_1(T)$. Duration is Erlang-distributed with shape $k_{I_1} = 2$. Agents with high clearance ability ($c_i > 0.5$) may recover early.

- **I_2 (Late infectious):** Symptomatic wasting with high shedding rate $\sigma_2(T)$. Duration is Erlang-distributed with shape $k_{I_2} = 2$. Agents may recover with probability $p_{\text{rec}} = \rho_{\text{rec}} \times c_i$ per day.

- **D (Dead from disease):** Carcass continues to shed pathogen saprophytically for a 3-day window at rate σ_D.

- **R (Recovered):** Immune; functionally equivalent to S for demographics but not susceptible to reinfection.

3.1.1 Erlang-Distributed Stage Durations

Durations in compartments E, I_1, and I_2 are drawn from Erlang distributions rather than geometric (exponential) distributions. The Erlang distribution with shape parameter k and rate parameter $k\mu$ has mean $1/\mu$ and coefficient of variation $\text{CV} = 1/\sqrt{k}$, producing more realistic, peaked duration distributions compared to the memoryless exponential [63]. For each individual entering a compartment, a duration is sampled as:

$$\tau \sim \text{Erlang}(k, \; k\mu(T)), \quad \text{rounded to} \quad \max(1, \; \text{round}(\tau)) \text{ days}, \tag{2}$$

where $\mu(T)$ is the temperature-dependent transition rate at the current SST (Section 3.3.2). The shape parameters are:

$$k_E = 3 \; (\text{CV} = 0.58), \quad k_{I_1} = 2 \; (\text{CV} = 0.71), \quad k_{I_2} = 2 \; (\text{CV} = 0.71). \tag{3}$$

Timers count down by one each day; when the timer reaches zero, the agent transitions to the next compartment.

3.2 Force of Infection

The per-individual instantaneous hazard rate of infection is:

$$\lambda_i = a_{\text{exp}} \underbrace{\frac{P_k}{K_{1/2} + P_k}}_{\text{dose–response}} \underbrace{(1 - r_i)}_{\text{resistance}} \underbrace{S_{\text{sal}}}_{\text{salinity}} \underbrace{f_{\text{size}}(L_i)}_{\text{size}}, \tag{4}$$

where:

- $a_{\text{exp}} = 0.75 \, \text{d}^{-1}$ is the baseline exposure rate;

15

- P_k is the local Vibrio concentration (bacteria mL^{-1}) at node k;

- $K_{1/2} = 87{,}000$ bacteria mL^{-1} is the half-infective dose (Michaelis–Menten dose–response);

- $r_i \in [0, 1]$ is the individual's resistance score (immune exclusion; Section 4);

- S_{sal} is the salinity modifier (Section 3.2.2);

- $f_{\mathrm{size}}(L_i)$ is the size-dependent susceptibility modifier (Section 3.2.3).

The discrete daily probability of infection is:

$$p_{\mathrm{inf}} = 1 - \exp(-\lambda_i \, \Delta t), \quad \Delta t = 1 \text{ day}. \tag{5}$$

3.2.1 Dose–Response Function

Pathogen exposure follows a Michaelis–Menten (saturating) dose–response:

$$D(P_k) = \frac{P_k}{K_{1/2} + P_k}. \tag{6}$$

At low concentrations ($P_k \ll K_{1/2}$), infection probability scales linearly with pathogen density; at high concentrations ($P_k \gg K_{1/2}$), it saturates at $D \to 1$, reflecting physiological limits on pathogen uptake.

3.2.2 Salinity Modifier

Vibrio viability is suppressed at low salinities, providing a mechanistic basis for the reduced SSWD prevalence observed in fjord systems:

$$S_{\mathrm{sal}} = \begin{cases} 0 & \text{if } S \leq S_{\min} = 10 \text{ psu}, \\ \left(\dfrac{S - S_{\min}}{S_{\mathrm{full}} - S_{\min}} \right)^{\eta} & \text{if } S_{\min} < S < S_{\mathrm{full}}, \\ 1 & \text{if } S \geq S_{\mathrm{full}} = 28 \text{ psu}, \end{cases} \tag{7}$$

where $\eta = 2$ produces a convex response (low salinity is strongly protective).

3.2.3 Size-Dependent Susceptibility

Larger *Pycnopodia helianthoides* are more susceptible to SSWD, consistent with the empirical finding of Eisenlord et al. [13] (odds ratio 1.23 per 10 mm increase in radius). The size modifier is:

$$f_{\mathrm{size}}(L_i) = \exp\left(\beta_L \, \frac{L_i - \bar{L}}{\sigma_L} \right), \tag{8}$$

where $\beta_L = 0.021\,\text{mm}^{-1}$ ($= \ln 1.23/10$), $\bar{L} = 300\,\text{mm}$ is the reference size, and $\sigma_L = 100\,\text{mm}$ normalizes the deviation. An individual of diameter $L_i = 500\,\text{mm}$ has $\sim 1.5\times$ the infection hazard of a $300\,\text{mm}$ individual.

3.2.4 Post-Spawning Immunosuppression

Spawning imposes a transient immune cost. Following each spawning event, an individual enters a 28-day immunosuppression window during which its effective resistance is reduced:

$$r_{i,\text{eff}} = \frac{r_i}{\psi_{\text{spawn}}}, \quad \psi_{\text{spawn}} = 2.0, \tag{9}$$

clamped to $[0, 1]$. This halves effective resistance during the immunosuppressed period, creating an evolutionary coupling between reproductive investment and disease vulnerability.

3.3 Disease Progression and Recovery

Disease progression rates are temperature-dependent via an Arrhenius function (Section 3.3.2). At each daily step, disease timers are decremented; when a timer reaches zero, the agent transitions to the next state. Recovery can occur before timer expiry.

3.3.1 Transition Rates

The base progression rates at reference temperature $T_{\text{ref}} = 20\,^\circ\text{C}$ are:

$$\mu_{E \to I_1} = 0.57\ \text{d}^{-1} \qquad\qquad (E_a/R = 4{,}000\ \text{K}), \tag{10}$$

$$\mu_{I_1 \to I_2} = 0.40\ \text{d}^{-1} \qquad\qquad (E_a/R = 5{,}000\ \text{K}), \tag{11}$$

$$\mu_{I_2 \to D} = 0.173\ \text{d}^{-1} \qquad\qquad (E_a/R = 2{,}000\ \text{K}). \tag{12}$$

The activation energy for $I_2 \to D$ is notably lower ($E_a/R = 2{,}000\,\text{K}$ vs. $5{,}000$–$6{,}000\,\text{K}$ for other transitions), reflecting evidence that terminal wasting is less temperature-sensitive than earlier disease stages (Errata E1).

3.3.2 Temperature Scaling (Arrhenius)

All temperature-dependent rates are scaled via the Arrhenius equation:

$$k(T) = k_{\text{ref}}\, \exp\left[\frac{E_a}{R}\left(\frac{1}{T_{\text{ref}}} - \frac{1}{T}\right)\right], \tag{13}$$

where $T_{\text{ref}} = 293.15\,\text{K}$ ($20\,^\circ\text{C}$) is the reference temperature corresponding to the *Vibrio pectenicida* thermal optimum [35], and E_a/R is the activation energy divided by the gas constant. The Arrhenius formulation ensures that colder temperatures slow disease

17

progression (longer E, I_1, I_2 durations) and reduce shedding rates, consistent with the observed latitudinal gradient in SSWD severity.

3.3.3 Tolerance: Extending I_2 Duration

The tolerance trait t_i operates as a damage-limitation mechanism that reduces the effective $I_2 \to D$ mortality rate, extending survival time while infected:

$$\mu_{I_2 \to D, \text{eff}} = \mu_{I_2 \to D}(T) \times (1 - t_i\,\tau_{\max}), \quad \text{floored at } 0.05 \times \mu_{I_2 \to D}(T), \tag{14}$$

where $\tau_{\max} = 0.85$ is the maximum mortality reduction at $t_i = 1$. The floor prevents biologically implausible indefinite survival. The effective rate is used when sampling the I_2 timer (Eq. 2), so tolerant individuals spend longer in I_2— which may prolong both recovery opportunity and pathogen shedding.

3.3.4 Recovery

Recovery from infection proceeds via the clearance trait c_i, which represents the host's capacity for pathogen elimination.

Recovery from I_2. Each day, an I_2 individual has probability:

$$p_{\text{rec},I_2} = \rho_{\text{rec}} \times c_i, \quad \rho_{\text{rec}} = 0.05 \text{ d}^{-1}, \tag{15}$$

of transitioning to the R compartment. At $c_i = 0$ (no clearance ability), recovery is impossible; at $c_i = 1$, the daily recovery probability is 5%.

Early recovery from I_1. Individuals with exceptionally high clearance ability ($c_i > 0.5$) can recover during the pre-symptomatic stage:

$$p_{\text{rec},I_1} = \begin{cases} 0 & \text{if } c_i \leq 0.5, \\ \rho_{\text{rec}} \times 2\,(c_i - 0.5) & \text{if } c_i > 0.5. \end{cases} \tag{16}$$

At $c_i = 1.0$, the early recovery probability equals ρ_{rec}, identical to I_2 recovery at maximum clearance. The threshold at $c_i = 0.5$ ensures that only rare, high-clearance individuals can clear infection before progressing to the symptomatic stage.

3.4 Vibrio Dynamics

The concentration of waterborne *Vibrio pectenicida* at node k evolves according to:

$$\frac{dP_k}{dt} = \underbrace{\sigma_1(T)\,n_{I_1} + \sigma_2(T)\,n_{I_2} + \sigma_D\,n_{D,\text{fresh}}}_{\text{shedding}} - \underbrace{\xi(T)\,P_k}_{\text{decay}} - \underbrace{\phi_k\,P_k}_{\text{flushing}} + \underbrace{P_{\text{env}}(T,S)}_{\text{reservoir}} + \underbrace{\sum_j d_{jk}\,P_j}_{\text{dispersal}},$$

(17)

integrated via forward Euler with $\Delta t = 1\,\text{day}$, subject to $P_k \geq 0$.

3.4.1 Shedding

Pathogen shedding from live infectious hosts is temperature-dependent:

$$\sigma_1(T) = 5.0 \times \text{Arr}(T) \quad (\text{I}_1: \text{pre-symptomatic}),$$

(18)

$$\sigma_2(T) = 50.0 \times \text{Arr}(T) \quad (\text{I}_2: \text{symptomatic}),$$

(19)

where $\text{Arr}(T)$ denotes the Arrhenius factor (Eq. 13) with $E_a/R = 5{,}000\,\text{K}$. The 10-fold difference between early and late shedding reflects the dramatic increase in tissue degradation and pathogen release during the wasting phase. Rates are given in bacteria $\text{mL}^{-1}\,\text{d}^{-1}\,\text{host}^{-1}$ and represent field-effective values (Errata E2).

3.4.2 Carcass Shedding

Dead individuals (D compartment) continue to shed pathogen saprophytically for a 3-day window at a constant rate $\sigma_D = 15\,\text{bacteria}\,\text{mL}^{-1}\,\text{d}^{-1}\,\text{carcass}^{-1}$ (field-effective; Code Errata CE-6). A ring buffer of daily disease death counts over the most recent 3 days tracks the number of "fresh" carcasses contributing to shedding:

$$n_{D,\text{fresh}}(t) = \sum_{\tau=0}^{2} \text{deaths}(t - \tau).$$

(20)

3.4.3 Vibrio Decay

Vibrio pectenicida survives longer in warmer water. The natural decay rate $\xi(T)$ is interpolated log-linearly between empirical estimates:

$$\xi(T) = \begin{cases} 1.0\,\text{d}^{-1} & T \leq 10\,°\text{C} \ (\text{half-life} \approx 0.7\,\text{d}), \\ 0.33\,\text{d}^{-1} & T \geq 20\,°\text{C} \ (\text{half-life} \approx 2.1\,\text{d}), \\ \exp\big[(1-f)\ln\xi_{10} + f\ln\xi_{20}\big] & \text{otherwise}, \end{cases}$$

(21)

where $f = (T-10)/10$ and values are clamped outside the 10–20 °C range. This counter-intuitive pattern (faster decay at cold temperatures) reflects the environmental Vibrio

19

508 literature [41].

3.4.4 Environmental Reservoir

In the ubiquitous scenario (default), *Vibrio pectenicida* is assumed to persist in the sediment as viable-but-non-culturable (VBNC) cells that resuscitate when SST exceeds a threshold. The background input rate is:

$$P_{\text{env}}(T, S) = P_{\text{env,max}} \underbrace{\frac{1}{1 + e^{-\kappa_{\text{VBNC}}\,(T - T_{\text{VBNC}})}}}_{\text{VBNC sigmoid}} \underbrace{g_{\text{peak}}(T)}_{\text{thermal performance}} \underbrace{S_{\text{sal}}}_{\text{salinity}}, \qquad (22)$$

where:

- $P_{\text{env,max}} = 500\,\text{bacteria}\,\text{mL}^{-1}\,\text{d}^{-1}$ is the maximum input rate;

- $\kappa_{\text{VBNC}} = 1.0\,^{\circ}\text{C}^{-1}$ controls the steepness of VBNC resuscitation;

- $T_{\text{VBNC}} = 12\,^{\circ}\text{C}$ is the midpoint temperature;

- $g_{\text{peak}}(T)$ is a thermal performance curve with Arrhenius increase below $T_{\text{opt}} = 20\,^{\circ}\text{C}$ and quadratic decline above, reaching zero at $T_{\text{max}} = 30\,^{\circ}\text{C}$.

In the invasion scenario, $P_{\text{env}} = 0$ everywhere until the pathogen is explicitly introduced.

3.5 Pathogen Evolution

When pathogen evolution is enabled, each infectious agent carries a continuous virulence phenotype v_i that modulates disease rates via mechanistic tradeoff functions.

3.5.1 Virulence–Tradeoff Curves

More virulent strains kill faster, shed more, and progress more rapidly, but also remove themselves from the host population sooner:

$$\sigma_{1,v}(T) = \sigma_1(T) \times \exp\!\big(\alpha_{\text{shed}}\,\gamma_{\text{early}}\,(v - v^*)\big), \qquad (23)$$

$$\sigma_{2,v}(T) = \sigma_2(T) \times \exp\!\big(\alpha_{\text{shed}}\,(v - v^*)\big), \qquad (24)$$

$$\mu_{I_1 \to I_2, v}(T) = \mu_{I_1 \to I_2}(T) \times \exp\!\big(\alpha_{\text{prog}}\,(v - v^*)\big), \qquad (25)$$

$$\mu_{I_2 \to D, v}(T) = \mu_{I_2 \to D}(T) \times \exp\!\big(\alpha_{\text{kill}}\,(v - v^*)\big), \qquad (26)$$

where $v^* = 0.5$ is the ancestral virulence (identity point), $\alpha_{\text{shed}} = 1.5$, $\alpha_{\text{prog}} = 1.0$, $\alpha_{\text{kill}} = 2.0$, and $\gamma_{\text{early}} = 0.3$ attenuates the shedding effect in the pre-symptomatic stage.

20

3.5.2 Transmission and Mutation

When a new infection occurs, the infecting strain is inherited either from a shedding individual (weighted by shedding rate) or from the environmental reservoir (with virulence $v_{\text{env}} = 0.5$). The probability of inheriting from a shedder is proportional to the total host-derived shedding relative to total pathogen input:

$$P(\text{from shedder}) = \frac{\sum_j \sigma_j(v_j, T)}{\sum_j \sigma_j(v_j, T) + P_{\text{env}}(T, S)}. \qquad (27)$$

The inherited virulence is then subject to mutation:

$$v_{\text{new}} = \text{clip}\big(v_{\text{parent}} + \mathcal{N}(0, \ \sigma_{v,\text{mut}}^2), \ v_{\text{min}}, \ v_{\text{max}}\big), \qquad (28)$$

with $\sigma_{v,\text{mut}} = 0.02$, $v_{\text{min}} = 0$, $v_{\text{max}} = 1$.

3.6 Basic Reproduction Number

The basic reproduction number provides a summary measure of epidemic potential at a node:

$$R_0 = \frac{a_{\text{exp}} \, S_0 \, (1 - \bar{r}) \, S_{\text{sal}}}{K_{1/2} \, (\xi(T) + \phi_k)} \left[\frac{\sigma_1(T)}{\mu_{I_1 \to I_2}(T)} + \frac{\sigma_2(T)}{\mu_{I_2 \to D,\text{eff}}(T) + \rho_{\text{rec}} \, \bar{c}} + \sigma_D \, \tau_D \right], \qquad (29)$$

where S_0 is the number of susceptibles, $\bar{r}$ and $\bar{c}$ are population-mean resistance and recovery scores, $\mu_{I_2 \to D,\text{eff}}$ incorporates population-mean tolerance (Eq. 14), $\rho_{\text{rec}} \, \bar{c}$ adds the recovery exit rate from I_2, and $\tau_D = 3 \, \text{days}$ is the carcass shedding duration. The three bracketed terms represent the pathogen contribution from each infectious compartment (I_1, I_2, and D carcasses, respectively).

3.7 Daily Update Sequence

Within each daily timestep, the disease module executes the following steps in order:

1. **Update Vibrio concentration** via Euler integration of Eq. 17, using current compartment counts and environmental conditions.

2. **Transmission (S $\to$ E):** For each susceptible agent, compute the force of infection λ_i (Eq. 4), convert to daily probability (Eq. 5), and draw a Bernoulli infection event. Newly exposed agents receive an Erlang-sampled E-stage timer. When pathogen evolution is active, the infecting strain is inherited and mutated (Section 3.5.2).

3. **Disease progression:** Decrement all disease timers. For agents with expired timers: E $\to$ I_1, $I_1 \to I_2$ (with tolerance-adjusted timer), $I_2 \to$ D. For agents with

21

active timers: check recovery from I_2 (Eq. 15) and early recovery from I_1 (Eq. 16).

4. **Carcass tracking:** Record today's disease deaths in the 3-day ring buffer for saprophytic shedding.

5. **Update diagnostics:** Recount compartments, update cumulative statistics (total infections, deaths, recoveries), track peak prevalence and peak Vibrio.

All operations are vectorized using NumPy batch sampling and array-level random draws for computational efficiency, achieving $O(N)$ scaling in population size.

4 Genetics Module

The genetics module tracks a diploid genotype at 51 biallelic loci for every individual, partitioned into three quantitative defense traits: *resistance*, *tolerance*, and *recovery*. Genotypes are transmitted via Mendelian inheritance with free recombination, mutated at a per-allele rate $\mu = 10^{-8}$ per generation [43], and subject to natural selection through the coupling of trait scores to disease dynamics (Section 3). The module additionally implements sweepstakes reproductive success (SRS) to capture the extreme reproductive variance characteristic of broadcast-spawning marine invertebrates [25].

4.1 Three-Trait Architecture

Each individual carries a (51×2) genotype array of `int8` alleles, where the 51 loci are partitioned into three contiguous blocks:

Table 3: Three-trait genetic architecture. The partition is configurable (constraint: $n_R + n_T + n_C = 51$); the default $17/17/17$ split is used in all analyses reported here.

Trait	Symbol	Loci	Indices	Mechanistic role
Resistance	r_i	$n_R = 17$	0–16	Immune exclusion: reduces probability of S $\to$ E transition
Tolerance	t_i	$n_T = 17$	17–33	Damage limitation: extends I_2 survival via mortality rate reduction
Recovery	c_i	$n_C = 17$	34–50	Pathogen clearance: daily probability of $I_1/I_2 \to$ R transition

These three traits represent biologically distinct immune strategies with different epidemiological consequences [50]:

- **Resistance** (r_i) acts *before* infection via receptor polymorphisms, barrier defenses, and innate pathogen recognition. Resistant individuals reduce pathogen pressure on the population by preventing shedding entirely.

22

- **Tolerance** (t_i) acts *during* infection via tissue repair, anti-inflammatory regulation, and metabolic compensation. Tolerant hosts survive longer while infected but continue to shed pathogen—they are epidemiological "silent spreaders" that maintain transmission pressure while saving themselves.

- **Recovery** (c_i) acts *during late infection* via coelomocyte phagocytosis and immune effector mobilization. Recovering hosts actively clear the pathogen and transition to an immune state (R), removing a shedding host from the population.

The locus count of 51 is motivated by Schiebelhut et al. [54], who identified $\sim$51 loci under selection in *Pisaster ochraceus* SSWD survivors. No genome-wide association study (GWAS) data currently distinguish resistance, tolerance, and recovery loci in *P. helianthoides*; the equal 17/17/17 partition is a simplifying assumption whose sensitivity is explored via the n_R parameter in the global sensitivity analysis (Section 7). A reference genome for *P. helianthoides* is now available [56], enabling future empirical partitioning.

Removal of EF1A overdominant locus. An earlier model version included a 52nd locus representing the EF1A elongation factor with overdominant fitness effects, based on Wares and Schiebelhut [62] who documented allele frequency shifts at this locus in *Pisaster ochraceus* following SSWD. We removed this locus because (1) the EF1A finding is specific to *Pisaster* with no evidence of overdominance in *P. helianthoides*, and (2) a single overdominant locus imposed a hard floor on heterozygosity loss that was biologically unjustified for our focal species.

4.2 Trait Score Computation

At each locus ℓ, an individual carries two alleles $g_{\ell,0}, g_{\ell,1} \in \{0,1\}$, where 1 denotes the derived (protective) allele and 0 the ancestral allele. Each locus within a trait block has a fixed effect size $e_\ell > 0$, and an individual's trait score is the effect-weighted mean allele dosage:

$$\theta_i = \sum_{\ell \in \mathcal{L}_\theta} e_\ell \frac{g_{\ell,0} + g_{\ell,1}}{2} \tag{30}$$

where $\mathcal{L}_\theta$ denotes the locus set for trait $\theta \in \{r, t, c\}$ and $\theta_i \in [0, \sum e_\ell]$. Effect sizes within each trait block are normalized so $\sum_{\ell \in \mathcal{L}_\theta} e_\ell = 1$, bounding all trait scores to $[0,1]$.

4.2.1 Effect Size Distribution

Per-locus effect sizes are drawn from an exponential distribution $e_\ell \sim \text{Exp}(\lambda = 1)$, normalized to sum to 1.0 within each trait, and sorted in descending order. This produces a distribution where a few loci have large effects and the remainder have small effects,

consistent with empirical QTL architectures for disease resistance traits [38]. A fixed seed ensures identical effect sizes across simulation runs. Each trait block receives independently drawn effect sizes.

4.2.2 Coupling to Disease Dynamics

The three traits feed into the disease module (Section 3) as follows:

1. **Resistance** reduces the per-individual force of infection:

$$\lambda_i = a \cdot \frac{P}{K_{1/2} + P} \cdot (1 - r_i) \cdot S_{\text{sal}} \cdot f_L(L_i) \tag{31}$$

where a is the exposure rate, P the local *Vibrio pectenicida* concentration, $K_{1/2}$ the half-infective dose, S_{sal} the salinity modifier, and $f_L(L_i)$ the size-dependent susceptibility factor.

2. **Tolerance** reduces the $I_2 \to D$ transition rate via a timer-scaling mechanism:

$$\mu_{\text{I}_2\text{D},i}^{\text{eff}} = \mu_{\text{I}_2\text{D}}(T) \cdot \left(1 - t_i \cdot \tau_{\max}\right) \tag{32}$$

where $\tau_{\max} = 0.85$ is the maximum mortality reduction achievable at $t_i = 1$. A floor of 5% of the baseline rate prevents complete elimination of disease mortality. Tolerant individuals survive longer while infected but continue shedding, creating a selective conflict between individual and population-level fitness.

3. **Recovery** determines the daily clearance probability:

$$p_{\text{rec},i} = \rho_{\text{rec}} \times c_i \tag{33}$$

where $\rho_{\text{rec}} = 0.05 \text{ d}^{-1}$ is the base recovery rate. Recovery from I_1 requires $c_i > 0.5$ (early clearance); recovery from I_2 has no threshold. Successful recovery transitions the agent to the R (recovered, immune) compartment.

4.3 Genotype Initialization

Initial allele frequencies are drawn independently for each locus from a Beta distribution:

$$q_\ell \sim \text{Beta}(a, b) \quad (\text{default } a = 2,\ b = 8) \tag{34}$$

producing a right-skewed frequency spectrum where most protective alleles are rare ($\mathbb{E}[q] = a/(a + b) = 0.2$), consistent with standing variation in immune genes maintained by mutation–selection balance. The raw frequencies are then rescaled per-trait so that the expected population-mean trait score equals a configurable target:

Table 4: Default target population-mean trait scores at initialization.

Trait	Target mean	Rationale
Resistance (r_i)	0.15	Pre-epidemic standing variation
Tolerance (t_i)	0.10	Moderate damage limitation
Recovery (c_i)	0.02	Rare standing variation for clearance

Recovery is initialized with the lowest mean because active pathogen clearance is assumed to be the rarest phenotype prior to epidemic exposure. Per-locus frequencies are clipped to $[0.001, 0.5]$ to prevent fixation at initialization while ensuring the derived allele never begins at majority frequency. Genotypes are then sampled assuming Hardy–Weinberg equilibrium at each locus: each allele copy is independently drawn as a Bernoulli trial with probability q_ℓ.

4.4   Mendelian Inheritance and Mutation

At reproduction, each offspring inherits one randomly chosen allele from each parent at every locus (independent assortment, no linkage). The vectorized implementation draws allele choices for all $n_{\text{offspring}} \times 51 \times 2$ positions simultaneously, then indexes into parental genotype arrays.

Mutations are applied to offspring genotypes at rate $\mu = 10^{-8}$ per allele per generation [43]. The total number of mutations per cohort is drawn from a Poisson distribution: $n_{\text{mut}} \sim \text{Pois}(\mu \times n_{\text{offspring}} \times 51 \times 2)$. Each mutation flips the allele at a randomly chosen position ($0 \to 1$ or $1 \to 0$), providing bidirectional mutational pressure. At the default mutation rate, mutations are negligible within the 20–100 year simulation horizon (expected $\sim 10^{-6}$ mutations per offspring), and evolution proceeds primarily through selection on standing variation.

4.5   Sweepstakes Reproductive Success

Broadcast-spawning marine invertebrates exhibit sweepstakes reproductive success (SRS): a tiny fraction of adults contribute the majority of surviving offspring in any given cohort [25]. This phenomenon produces N_e/N ratios on the order of 10^{-3} in empirical observations [3] and dramatically amplifies genetic drift while simultaneously accelerating the fixation of favorable alleles in post-epidemic populations [14].

SSWD-EvoEpi implements SRS via a Pareto-weighted reproductive lottery. Each spawning adult receives a random weight drawn from a Pareto distribution with shape parameter α_{SRS} (default 1.35):

$$w_i \sim \text{Pareto}(\alpha_{\text{SRS}}) + 1 \tag{35}$$

Female weights are additionally multiplied by size-dependent fecundity (Section 5.5), so larger females that win the sweepstakes lottery contribute disproportionately:

$$\tilde{w}_{i,\text{female}} = w_i \times \left(\frac{L_i}{L_{\text{ref}}}\right)^b \tag{36}$$

where $b = 2.5$ is the fecundity allometric exponent and $L_{\text{ref}} = 500$ mm. Male weights use the raw Pareto draw without fecundity modulation. Parents are then sampled with replacement from the normalized weight distributions, and offspring receive Mendelian-inherited genotypes.

The Pareto shape $\alpha_{\text{SRS}} = 1.35$ was chosen to produce N_e/N ratios consistent with empirical estimates of $\sim 10^{-3}$ in marine broadcast spawners [3, 25]. A small annual variation in α (drawn from $\mathcal{N}(\alpha_{\text{SRS}}, \sigma_\alpha^2)$ with $\sigma_\alpha = 0.10$) produces temporal fluctuation in the variance of reproductive success across cohorts.

Effective population size. N_e is computed from the realized offspring distribution using the standard formula [25]:

$$N_e = \frac{4N - 2}{V_k + 2} \tag{37}$$

where N is the number of spawning parents and V_k is the variance in offspring number. Sex-specific N_e values are computed for females and males separately, then combined via harmonic mean: $N_e = 4N_{e,f} N_{e,m}/(N_{e,f} + N_{e,m})$.

4.6 Genetic Diagnostics and Tracking

The model records a suite of genetic summary statistics at each node at annual intervals:

- **Per-trait means and variances:** $\bar{r}$, $\bar{t}$, $\bar{c}$ and $\text{Var}(r)$, $\text{Var}(t)$, $\text{Var}(c)$.

- **Additive genetic variance** (V_A) per trait:

$$V_{A,\theta} = \sum_{\ell \in \mathcal{L}_\theta} 2 \, e_\ell^2 \, q_\ell \, (1 - q_\ell) \tag{38}$$

  where q_ℓ is the derived allele frequency at locus ℓ. V_A determines the potential rate of evolutionary response to selection.

- **Heterozygosity:** Observed (H_o) and expected (H_e) heterozygosity averaged across all 51 loci.

- F_{ST}**:** Weir–Cockerham-style F_{ST} across nodes, computed as $F_{ST} = \text{Var}(\bar{q})/[\bar{q}(1-\bar{q})]$ averaged across polymorphic loci.

26

- **Pre- and post-epidemic allele frequency snapshots:** Full 51-locus allele frequency vectors taken immediately before pathogen introduction and two years after the epidemic onset, enabling direct measurement of allele frequency shifts (Δq) attributable to selection.

No cost of resistance. A cost-of-resistance parameter (fecundity penalty for high r_i) was considered but excluded following discussion with the senior author. No empirical evidence supports a measurable fecundity cost for disease resistance alleles in *P. helianthoides*, and including an unparameterized cost would introduce a free parameter with no calibration target. Fecundity depends solely on body size (Section 5.5).

4.7 Genotype Bank (Tier 2 Nodes)

For Tier 2 spatial nodes that use simplified demographics rather than full agent tracking, the genetics module maintains a *genotype bank* of $N_{\text{bank}} = 100$ representative diploid genotypes with associated frequency weights. The bank is created by random sampling from the alive population and preserves all three trait scores and allele frequencies. When agents migrate from a Tier 2 to a Tier 1 node, genotypes are expanded from the bank using SRS-weighted sampling (Pareto weights × bank frequency weights) to reconstruct individual-level genetic variation.

5 Population Dynamics

The population dynamics module governs the complete life history of *Pycnopodia helianthoides*: growth, natural mortality, reproduction, larval dispersal, and settlement. All demographic processes operate on a daily timestep, integrated within the master simulation loop described in Section 2. Disease-driven mortality is handled by the disease module (Section 3); coupling occurs through shared access to the agent array.

5.1 Life Stages

Each individual progresses through five life stages defined by size thresholds (Table 5). Stage transitions are unidirectional: agents can only advance, never regress.

Table 5: Life stages and transition thresholds for *P. helianthoides*.

Stage	Size range	Transition at	Duration
Egg/Larva	Planktonic	Settlement event	49–146 days PLD
Settler	0.5–10 mm	≥ 10 mm	~1 year
Juvenile	10–150 mm	≥ 150 mm	~1–5 years
Subadult	150–400 mm	≥ 400 mm	~5–10 years
Adult	>400 mm	—	10–50+ years

5.2 Growth

Individual growth follows the von Bertalanffy (VB) growth model in differential form, resolved daily:

$$L(t + \Delta t) = L_\infty - (L_\infty - L(t)) \cdot \exp(-k_{\text{growth}} \cdot \Delta t) \tag{39}$$

where $L_\infty = 1000$ mm is the asymptotic arm-tip diameter, $k_{\text{growth}} = 0.08$ yr^{-1} is the Brody growth coefficient, and $\Delta t = 1/365$ yr for the daily timestep. Individual growth variation is introduced through a multiplicative log-normal noise term applied to the daily increment:

$$\Delta L_i = (L_{\text{det}} - L_i) \cdot \exp(\varepsilon_i), \quad \varepsilon_i \sim \mathcal{N}\left(0, \ \frac{\sigma_g}{\sqrt{365}}\right) \tag{40}$$

where $\sigma_g = 2.0$ mm is the annual growth noise scale and the $\sqrt{365}$ scaling preserves the annual CV when integrated over daily steps. Size is constrained to never decrease (no shrinking). Stage transitions are evaluated after each growth step based on the thresholds in Table 5.

Aging proceeds at $1/365$ years per day, producing fractional ages that drive size-at-age trajectories and determine eligibility for senescence mortality.

5.3 Natural Mortality

Natural mortality is resolved daily using continuous hazard rates derived from stage-specific annual survival probabilities. The daily death probability for individual i is:

$$p_{\text{death},i} = 1 - \left(1 - m_{\text{annual}}(s_i)\right)^{1/365} \tag{41}$$

where $m_{\text{annual}}(s) = 1 - S_{\text{annual}}(s)$ is the annual mortality rate for stage s. The annual survival schedule (Table 6) produces a type III survivorship curve with high settler/juvenile mortality and low adult mortality, consistent with demographic estimates for long-lived asteroids.

Table 6: Stage-specific annual survival rates.

Stage	Annual survival (S)	Annual mortality
Settler	0.001	0.999
Juvenile	0.03	0.97
Subadult	0.90	0.10
Adult	0.95	0.05
Senescent	0.98	0.02 (base)

Senescence. Individuals exceeding the senescence age ($a_{\mathrm{sen}} = 50$ yr) accumulate additional mortality linearly:

$$m_{\mathrm{total}}(s_i, a_i) = m_{\mathrm{annual}}(s_i) + m_{\mathrm{sen}} \cdot \frac{a_i - a_{\mathrm{sen}}}{20} \tag{42}$$

where $m_{\mathrm{sen}} = 0.10$ and the divisor of 20 scales the senescence ramp such that a 70-year-old individual experiences an additional 10% annual mortality.

Daily mortality is applied via a single vectorized random draw across all alive agents, converting stage-dependent annual rates to daily hazard probabilities. This continuous approach avoids the artificial synchronization artifacts of annual batch mortality and permits realistic within-year population fluctuations.

5.4 Spawning System

SSWD-EvoEpi implements a biologically detailed spawning system reflecting the extended reproductive season and cascading spawning behavior observed in *P. helianthoides*.

5.4.1 Spawning Season and Phenology

The spawning season extends from day 305 ($\approx$November 1) through day 196 ($\approx$July 15) of the following year, spanning approximately 270 days and wrapping across the calendar year boundary. Spawning intensity follows a Normal envelope centered on a latitude-adjusted peak:

$$P_{\mathrm{season}}(d) = \exp\left(-\frac{(\Delta d)^2}{2\,\sigma_{\mathrm{peak}}^2}\right) \tag{43}$$

where Δd is the shortest circular distance between day d and the peak day (accounting for year wrapping), and $\sigma_{\mathrm{peak}} = 60$ days is the standard deviation of the seasonal peak. The peak day-of-year is latitude-dependent:

$$d_{\mathrm{peak}}(\phi) = d_{\mathrm{peak,base}} + \lceil (\phi - 40°\mathrm{N}) \times 3\ \mathrm{d}/° \rceil \tag{44}$$

where $d_{\text{peak,base}} = 105$ ($\approx$April 15) is the reference peak at 40°N, and higher-latitude populations spawn approximately 3 days later per degree northward.

5.4.2 Spontaneous Spawning

Each day during the spawning season, mature adults ($\geq$400 mm, Susceptible or Recovered disease state) are first evaluated for *readiness*, a stochastic physiological state modulated by the seasonal envelope $P_{\text{season}}(d)$. Once ready, individuals attempt spontaneous spawning with sex-specific daily probabilities:

$$p_{\text{spawn,female}} = 0.012 \tag{45}$$

$$p_{\text{spawn,male}} = 0.0125 \tag{46}$$

These rates were calibrated to produce $\geq$80% female spawning participation per season and a mean of $\sim$2.2 male bouts per season, consistent with the observation that males spawn more frequently than females in broadcast-spawning asteroids.

Bout limits and refractory periods. Females are limited to a maximum of 2 spawning bouts per season; males are limited to 3 bouts. Males enter a brief refractory period between bouts (default 0 days, configurable) during which they cannot spawn, reflecting the physiological recovery time for spermatogenesis.

5.4.3 Cascade Induction

Spawning by one individual can trigger spawning in nearby conspecifics via waterborne chemical cues (spawning-induced spawning), producing the synchronous mass spawning events observed in broadcast spawners. Induction operates over a 3-day chemical cue persistence window and is strongly sex-asymmetric:

$$\kappa_{\text{fm}} = 0.80 \quad \text{(female} \rightarrow \text{male induction)} \tag{47}$$

$$\kappa_{\text{mf}} = 0.60 \quad \text{(male} \rightarrow \text{female induction)} \tag{48}$$

where κ_{fm} is the probability that a ready male spawns when a female within the cascade radius (200 m) has spawned within the cue window. The female-to-male asymmetry reflects the stronger spawning trigger provided by egg-associated chemical signals. Readiness induction also operates: individuals not yet physiologically ready can be driven to readiness by nearby spawning activity, with a daily probability of 0.5 when within a 300 m detection radius.

5.4.4 Post-Spawning Immunosuppression

Spawning imposes a 28-day immunosuppression period during which the individual's force of infection is multiplied by a susceptibility factor of 2.0:

$$\lambda_i^{\text{eff}} = \lambda_i \times \begin{cases} \chi_{\text{immuno}} = 2.0 & \text{if immunosuppression timer} > 0 \\ 1.0 & \text{otherwise} \end{cases} \tag{49}$$

This reflects the metabolic cost of gamete production and the documented increase in disease susceptibility following reproductive investment in marine invertebrates. The immunosuppression timer is reset each time an individual spawns, so multiple spawning bouts within a season extend the vulnerability window. Immunosuppression timers are decremented daily regardless of spawning season status.

5.5 Fecundity

Female fecundity follows an allometric relationship with body size:

$$F_i = F_0 \cdot \left(\frac{L_i}{L_{\text{ref}}} \right)^b \tag{50}$$

where $F_0 = 10^7$ eggs is the reference fecundity at $L_{\text{ref}} = 500$ mm and $b = 2.5$ is the allometric exponent. Only females at or above the minimum reproductive size $L_{\text{min}} = 400$ mm produce eggs. No cost-of-resistance penalty is applied to fecundity (Section 4.6).

5.6 Fertilization Kinetics and the Allee Effect

Broadcast spawners face a fertilization Allee effect: at low population density, sperm limitation reduces the fraction of eggs successfully fertilized [16, 40]. We model fertilization success using a mean-field approximation of the Lundquist and Botsford [40] broadcast fertilization model:

$$\mathcal{F}(\rho_m) = 1 - \exp(-\gamma_{\text{fert}} \cdot \rho_{m,\text{eff}}) \tag{51}$$

where $\gamma_{\text{fert}} = 4.5$ m^2 is the sperm contact parameter and $\rho_{m,\text{eff}}$ is the effective male density, potentially enhanced by spawning aggregation behavior. The aggregation factor increases effective local density within spawning clumps above the spatially uniform average when adult count exceeds a threshold.

This produces a quadratic relationship between zygote production and density at low density: zygotes $\propto \rho_f \times \mathcal{F}(\rho_m) \propto \rho^2$ when $\rho \to 0$, creating a strong demographic Allee effect. For high-fecundity broadcast spawners like *P. helianthoides*, the deterministic Allee threshold is near zero density; the practical Allee effect operates through stochastic processes at low N.

31

5.7 Larval Phase

Fertilized eggs enter a temperature-dependent pelagic larval duration (PLD):

$$\mathrm{PLD}(T) = \mathrm{PLD}_{\mathrm{ref}} \cdot \exp\!\big(-Q_{\mathrm{dev}} \cdot (T - T_{\mathrm{ref}})\big) \tag{52}$$

where $\mathrm{PLD}_{\mathrm{ref}} = 63$ days at $T_{\mathrm{ref}} = 10.5°\mathrm{C}$ [33], and $Q_{\mathrm{dev}} = 0.05$ $°\mathrm{C}^{-1}$ produces shorter PLD at warmer temperatures. PLD is clamped to $[30, 150]$ days.

Larval survival during the pelagic phase follows a constant daily mortality model:

$$S_{\mathrm{larval}} = \exp(-\mu_{\mathrm{larva}} \cdot \mathrm{PLD}) \tag{53}$$

with $\mu_{\mathrm{larva}} = 0.05$ d^{-1}. At the reference PLD of 63 days, this yields $S_{\mathrm{larval}} \approx 4.3\%$ — high mortality that is compensated by the enormous fecundity of *P. helianthoides*.

Larval cohorts carry genotypes inherited via the SRS lottery (Section 4.5) and are tracked as discrete objects during the pelagic phase. Upon completion of PLD, competent larvae are available for settlement. In the spatial simulation (Section 6), cohorts are dispersed between nodes via the larval connectivity matrix $\mathbf{C}$ before settlement.

5.8 Settlement and Recruitment

Competent larvae settle into the benthic population through a three-stage process:

1. Settlement cue (Allee effect). Settlement success is modulated by the presence of conspecific adults via a Michaelis–Menten function representing biofilm-mediated settlement cues:

$$C_{\mathrm{settle}}(N_{\mathrm{adults}}) = 0.2 + \frac{0.8 \cdot N_{\mathrm{adults}}}{5 + N_{\mathrm{adults}}} \tag{54}$$

where the baseline of 0.2 represents settlement on coralline algae in the absence of adults, and the additional 0.8 reflects enhanced settlement induced by adult biofilm. The half-saturation constant of 5 adults means that even a small remnant population provides strong settlement cues.

2. Density-dependent recruitment (Beverton–Holt). The number of recruits is governed by a standard Beverton–Holt stock-recruitment relationship:

$$R = \frac{K \cdot s_0 \cdot S}{K + s_0 \cdot S} \tag{55}$$

where S is the number of effective settlers (after cue modulation), K is the carrying capacity, and $s_0 = 0.03$ is the density-independent per-settler survival rate. At low S,

32

$R \approx s_0 S$ (supply-limited); at high S, $R \to K$ (habitat-limited). For broadcast spawners with $S \gg K$, recruitment is typically habitat-limited and population self-regulates.

3. Agent initialization. Recruited settlers are placed in dead agent slots, assigned size 0.5 mm, age 0, Settler stage, random sex (1:1 ratio), Susceptible disease state, and random position within the node's habitat area. Genotypes are copied from the SRS-selected settler genotypes, and all three trait scores (r_i, t_i, c_i) are computed from the inherited genotype.

Juvenile immunity. Newly settled individuals can optionally be granted a juvenile immunity period (configurable, default 0 days) during which they are not susceptible to infection. The settlement day is recorded for each recruit to enable age-dependent susceptibility calculations.

5.9 Continuous Settlement

Rather than settling all larvae in an annual pulse, the model tracks individual larval cohorts and settles them daily as their PLD elapses. Cohorts generated by daily spawning events throughout the extended spawning season (Section 5.4.1) are stored in a per-node pending list sorted by settlement day. Each simulation day, cohorts whose PLD has elapsed are popped from the sorted list front (amortized $O(1)$) and passed through the settlement pipeline. This continuous approach produces realistic seasonal recruitment pulses that peak several months after the spawning peak, consistent with the observed temporal offset between spawning and juvenile recruitment in *P. helianthoides*.

At the annual boundary, any remaining unsettled cohorts from each node are collected for spatial dispersal via the connectivity matrix **C** (Section 6), then redistributed to destination nodes where they continue to settle daily as PLD elapses.

5.10 Demographic–Genetic–Epidemiological Coupling

The population dynamics module is bidirectionally coupled to the disease and genetics modules:

- **Disease $\to$ demographics:** Disease kills individuals ($I_2 \to D$), reducing population size and altering age/size structure. Post-spawning immunosuppression (Section 5.4.4) increases disease risk for recent spawners, creating a temporal alignment between peak reproductive effort and peak epidemic severity during warm months.

- **Demographics $\to$ disease:** Reduced population density lowers contact rates and environmental pathogen concentration. The fertilization Allee effect (Section 5.6)

amplifies population collapse by reducing reproductive output at low density, potentially trapping populations in an extinction vortex.

- **Genetics → demographics:** The SRS lottery (Section 4.5) produces extreme reproductive variance that amplifies genetic drift while accelerating the fixation of resistance, tolerance, and recovery alleles enriched by selection during epidemic episodes.

- **Demographics → genetics:** Population bottlenecks from disease reduce N_e far below census N, compounded by SRS ($N_e/N \sim 10^{-3}$). The interaction of selection with small effective population size determines whether evolutionary rescue is fast enough to prevent extinction.

6 Spatial Module and Environmental Forcing

SSWD-EvoEpi represents the NE Pacific range of *Pycnopodia helianthoides* as a metapopulation network of discrete spatial nodes connected by larval dispersal and pathogen transport. Each node carries its own environmental forcing (sea surface temperature, salinity, flushing rate) that modulates local disease and demographic dynamics. This section describes the spatial architecture, connectivity matrices, environmental time series, and agent movement model.

6.1 Metapopulation Network Structure

The metapopulation is a graph $\mathcal{G} = (\mathcal{N}, \mathbf{C}, \mathbf{D})$ where each node $k \in \mathcal{N}$ represents a geographically delineated habitat patch and $\mathbf{C}, \mathbf{D}$ are the larval and pathogen connectivity matrices, respectively.

6.1.1 Node Definition

Each node is parameterized by a `NodeDefinition` record with the following fields:

Table 7: Node definition fields.

Field	Units	Description
lat, lon	°N, °E	Geographic coordinates
carrying_capacity	individuals	Local K (= habitat area $\times \rho_{\max}$)
is_fjord	bool	Fjord vs. open coast classification
sill_depth	m	Sill depth (∞ for open coast)
flushing_rate	d^{-1}	Mean annual hydrodynamic flushing ϕ_k
mean_sst	°C	Baseline annual mean SST
sst_amplitude	°C	Annual cycle half-range
sst_trend	$°C\,yr^{-1}$	Linear warming trend
salinity	psu	Effective mean salinity
depth_range	m	Min–max habitat depth
subregion	—	Biogeographic subregion code

At runtime, each `NodeDefinition` is wrapped in a `SpatialNode` object that holds the local population arrays (agents and genotypes), current environmental state (SST, salinity, flushing rate), Vibrio concentration, and diagnostic flags. The `MetapopulationNetwork` aggregates all nodes together with the **C**, **D**, and distance matrices.

6.1.2 Internode Distance Computation

Connectivity kernels require pairwise waterway distances between nodes. Two methods are available:

Haversine with tortuosity. For small networks (≤ 11 nodes), geodesic great-circle distances are computed via the Haversine formula and multiplied by a uniform tortuosity factor $\tau = 1.5$ (intermediate between open-coast ~ 1.2 and fjord ~ 2.5) to approximate along-coast path lengths:

$$d_{jk}^{\text{water}} = \tau \times d_{jk}^{\text{Haversine}}. \tag{56}$$

Precomputed overwater distances. For full-range simulations, a 489-site overwater distance matrix was computed from GEBCO 2022 bathymetric data at 15 arc-second resolution. Land cells were rasterized from Natural Earth 10 m land polygons, and Dijkstra's algorithm on a 4-connected ocean grid yielded shortest overwater paths. The resulting 489×489 matrix spans 2.0–7,187 km, with 98.4% of pairs connected (1,946 disconnected pairs involve western Aleutian sites near the antimeridian). Model nodes are matched to the nearest precomputed site within a 50 km tolerance; unmatched nodes fall back to Haversine $\times \tau$.

6.2 Connectivity Matrices

Two connectivity matrices govern inter-node exchange: $\mathbf{C}$ for annual larval dispersal and $\mathbf{D}$ for daily pathogen transport (Errata E5). Both use exponential distance kernels but operate at different spatial and temporal scales.

6.2.1 Larval Connectivity Matrix C

C_{jk} gives the probability that a competent larva produced at node j settles at node k. The matrix is constructed from an exponential dispersal kernel with explicit self-recruitment:

$$C_{jk} = \begin{cases} \alpha_j & \text{if } j = k, \\ (1 - \alpha_j) \exp\left(-\dfrac{d_{jk}}{D_L}\right) b_{jk} & \text{if } j \neq k, \end{cases} \tag{57}$$

where:

- $D_L = 400\,\text{km}$ is the larval dispersal length scale, reflecting the 4–8 week pelagic larval duration (PLD) of *Pycnopodia helianthoides* [?];

- α_j is the self-recruitment fraction: $\alpha_{\text{fjord}} = 0.30$ for fjord nodes (reflecting enhanced retention behind sills) and $\alpha_{\text{open}} = 0.10$ for open-coast nodes;

- $b_{jk} \in [0, 1]$ is an optional barrier attenuation factor for biogeographic breaks (e.g., Cape Mendocino).

Rows are then normalized so that:

$$\sum_k C_{jk} = r_{\text{total}} = 0.02, \tag{58}$$

where r_{total} represents the total per-larva settlement success probability, accounting for the compounding losses of pelagic mortality, failed metamorphosis, and post-settlement predation.

The elevated self-recruitment fraction for fjord nodes ($\alpha_{\text{fjord}} = 3\alpha_{\text{open}}$) encodes the empirical observation that fjords act as larval retention zones [?]: sill-mediated circulation traps larvae near their natal site, reducing export to the open coast.

6.2.2 Pathogen Dispersal Matrix D

D_{jk} gives the fraction of waterborne *Vibrio pectenicida* at node j that reaches node k per day. Pathogen dispersal operates at much shorter range than larval dispersal:

$$D_{jk} = \phi_j \, f_{\text{out}} \, \exp\left(-\frac{d_{jk}}{D_P}\right) S_{jk} \quad \text{for} \quad d_{jk} \leq 50 \text{ km}, \tag{59}$$

where:

- $D_P = 15\,\mathrm{km}$ is the pathogen dispersal scale (reflecting tidal-current transport);

- ϕ_j is the source node's flushing rate (d^{-1});

- $f_{\mathrm{out}} = 0.2$ is the fraction of flushed water reaching neighboring sites;

- S_{jk} is the sill attenuation factor.

Pairs beyond $d_{jk} > 50\,\mathrm{km}$ receive zero pathogen transfer. Total export from any node is capped at its flushing rate: $\sum_k D_{jk} \leq \phi_j$.

Sill attenuation. Fjord sills impede pathogen exchange between basins. The attenuation factor is computed from the minimum sill depth across the pair:

$$S_{jk} = \min\left(1, \left[\frac{\min(z_j^{\mathrm{sill}}, z_k^{\mathrm{sill}})}{\max(z_j^{\mathrm{max}}, z_k^{\mathrm{max}})}\right]^2\right), \tag{60}$$

where z^{sill} is sill depth and z^{max} is maximum habitat depth. For open-coast nodes ($z^{\mathrm{sill}} = \infty$), $S_{jk} = 1$ (no attenuation). For Howe Sound (sill $= 30\,\mathrm{m}$, max depth $= 100\,\mathrm{m}$), $S \approx 0.09$, reducing pathogen exchange by $\sim 91\%$.

6.2.3 Dispersal Dynamics

Pathogen dispersal (daily). At each timestep, the dispersal input to node k is:

$$\Delta P_k^{\mathrm{dispersal}} = \sum_j D_{jk}\, P_j = \left(\mathbf{D}^\top \mathbf{P}\right)_k, \tag{61}$$

which enters the Vibrio ODE (Eq. 17) as an additive source term.

Larval dispersal (annual). At the end of each reproductive season, competent larvae from each source node are distributed to receiving nodes via $\mathbf{C}$. For source node j producing n_j competent larvae: (i) a binomial draw $n_{\mathrm{settle}} \sim \mathrm{Bin}(n_j, \sum_k C_{jk})$ determines total settlement; (ii) a multinomial draw allocates settlers across destinations proportional to the conditional probabilities $C_{jk}/\sum_k C_{jk}$; (iii) settler genotypes are sampled with replacement from the source pool.

6.3 Environmental Forcing

Each node receives a locally parameterized environmental forcing that drives disease and demographic rates through temperature-dependent, salinity-dependent, and flushing-dependent mechanisms.

6.3.1 Sea Surface Temperature

Daily SST at node k follows a sinusoidal annual cycle with a linear warming trend and optional stochastic perturbation:

$$T_k(d, y) = \underbrace{\bar{T}_k + \gamma_k \left(y - y_{\text{ref}}\right)}_{\text{trend-adjusted mean}} + \underbrace{A_k \cos\left(\frac{2\pi \left(d - d_{\text{peak}}\right)}{365}\right)}_{\text{annual cycle}}, \qquad (62)$$

where:

- $\bar{T}_k$ is the baseline annual mean SST (°C) at reference year $y_{\text{ref}} = 2000$;

- A_k is the annual cycle half-range (°C);

- γ_k is the linear warming rate (°C yr^{-1}; default 0.02);

- $d_{\text{peak}} = 227$ (day of year $\approx$ August 15) corresponds to the late-summer SST maximum characteristic of the NE Pacific.

The warming trend shifts the SST climatology upward over time, increasing both baseline Vibrio viability and the duration of the high-risk summer window. For the 5-node validation network, $\bar{T}_k$ ranges from 8.0 °C (Sitka) to 14.0 °C (Monterey), producing a ~6 °C latitudinal gradient consistent with satellite SST climatologies.

SST time series are precomputed at initialization via `make_sst_timeseries` and stored as dense 1-D arrays of shape $(n_{\text{years}} \times 365)$ for efficient daily lookup.

6.3.2 Temperature-Dependent Rate Scaling

All temperature-dependent biological rates—disease progression, pathogen shedding, Vibrio decay—are scaled via the Arrhenius function:

$$k(T) = k_{\text{ref}} \ \exp\left[\frac{E_a}{R}\left(\frac{1}{T_{\text{ref}}} - \frac{1}{T}\right)\right], \qquad (63)$$

with $T_{\text{ref}} = 293.15$ K (20 °C), the thermal optimum of *Vibrio pectenicida* [35]. This formulation ensures that the latitudinal SST gradient (Eq. 62) produces emergent north–south gradients in disease severity, matching the observed pattern of southward-increasing SSWD mortality during the 2013–2015 outbreak [? ?].

38

6.3.3 Salinity Modifier

Vibrio viability is suppressed at low salinities via a quadratic ramp (Eq. 7), reproduced here for completeness:

$$S_{\text{sal}} = \text{clip}\left(\left[\frac{S_k - S_{\min}}{S_{\text{full}} - S_{\min}}\right]^2, \, 0, \, 1\right), \quad S_{\min} = 10 \text{ psu}, \quad S_{\text{full}} = 28 \text{ psu}. \tag{64}$$

Fjord nodes receive lower salinities (e.g., Howe Sound $S = 22$ psu due to freshwater runoff), yielding $S_{\text{sal}} = 0.44$ and reducing effective Vibrio viability by $\sim 56\%$ compared to open-coast nodes ($S \geq 30$ psu, $S_{\text{sal}} \geq 0.87$). This mechanism provides a partial explanation for fjord refugia observations [?].

6.3.4 Flushing Rate

Hydrodynamic flushing removes waterborne pathogen at rate ϕ_k (d^{-1}), entering the Vibrio ODE as the term $-\phi_k P_k$ (Eq. 17). Node-specific values span two orders of magnitude:

- Open coast: $\phi_k = 0.5$–$1.0 \, \text{d}^{-1}$ (strong tidal and current flushing);

- Semi-enclosed bays: $\phi_k = 0.3 \, \text{d}^{-1}$ (San Juan Islands);

- Fjords: $\phi_k = 0.007$–$0.05 \, \text{d}^{-1}$ (Errata E3; sill restricts water exchange). Howe Sound is assigned $\phi_k = 0.03 \, \text{d}^{-1}$.

Low flushing in fjords acts as a double-edged mechanism: it reduces the rate of pathogen removal (potentially increasing local Vibrio concentrations) but also reduces pathogen *export* to neighboring nodes via $\mathbf{D}$ (Eq. 59), effectively isolating the fjord from regional epidemic dynamics.

Flushing rates are optionally modulated seasonally:

$$\phi_k(m) = \bar{\phi}_k \left[1 + A_\phi \cos\left(\frac{2\pi (m - 5)}{12}\right)\right], \tag{65}$$

where m is the 0-indexed month, $A_\phi = 0.3$ for fjord nodes and $A_\phi = 0.2$ for open coast, with peak flushing in June ($m = 5$) corresponding to freshwater-driven estuarine circulation maxima.

6.4 Agent Movement

Within each node, agents move via a correlated random walk (CRW) that produces realistic small-scale spatial structure:

$$\theta(t + \Delta t) = \theta(t) + \mathcal{N}(0, \sigma_\theta^2), \tag{66}$$

$$x(t + \Delta t) = x(t) + v_i \cos\theta \, \Delta t, \tag{67}$$

$$y(t + \Delta t) = y(t) + v_i \sin\theta \, \Delta t, \tag{68}$$

where $\sigma_\theta = 0.6\,\mathrm{rad}$ is the turning-angle standard deviation, $v_i = v_{\mathrm{base}} \times m_{\mathrm{state}}$ is the disease-modified speed, and $\Delta t = 60\,\mathrm{min}$ (hourly substeps, 24 per day). The base speed $v_{\mathrm{base}} = 0.5\,\mathrm{m\,min}^{-1}$ is consistent with undisturbed *Pycnopodia helianthoides* locomotion rates [?]. Disease state modifies speed: $m_S = m_E = 1.0$ (healthy), $m_{I_1} = 0.5$ (mild impairment), $m_{I_2} = 0.1$ (severe wasting), $m_D = 0.0$ (stationary carcass), $m_R = 1.0$ (recovered).

Agents are confined to a square habitat of side length $\sqrt{\mathrm{habitat\_area}}$ with elastic boundary reflection.

Spatial transmission. When spatial transmission is enabled, each node's habitat is discretized into a grid with cell size $\Delta x = 20\,\mathrm{m}$. Infected agents deposit pathogen exposure proportional to their shedding rate into their grid cell, and two Gaussian diffusion passes (3×3 averaging) smooth the resulting density field. Susceptible agents then experience locally elevated or reduced force of infection depending on their proximity to infected individuals, creating emergent disease clustering without modifying the node-level Vibrio ODE.

Sensitivity analysis substeps. The full 24 hourly substeps per day incur ∼20× computational overhead. For sensitivity analysis runs (Section **??**), movement is reduced to 1 substep per day, which captures spatial mixing and aggregation effects at acceptable cost.

6.5 Network Configurations

Three network configurations are used across model development, validation, and sensitivity analysis.

6.5.1 5-Node Validation Network

The primary validation network spans the NE Pacific range with five nodes selected to represent key biogeographic contexts (Table 8):

Table 8: 5-node validation network configuration. SST parameters are baseline values at reference year 2000.

Node	Lat	Lon	$\bar{T}$ (°C)	A (°C)	S (psu)	ϕ (d^{-1})
Sitka, AK	57.06	−135.34	8.0	3.5	32.0	0.80
Howe Sound, BC	49.52	−123.25	10.0	4.0	22.0	0.03
San Juan Is, WA	48.53	−123.02	10.0	4.0	30.0	0.30
Newport, OR	44.63	−124.05	12.0	3.0	33.0	1.00
Monterey, CA	36.62	−121.90	14.0	2.5	33.5	0.80

Howe Sound is the sole fjord node (sill depth $= 30\,\mathrm{m}$, $\alpha_{\mathrm{self}} = 0.30$); all others are open coast ($\alpha_{\mathrm{self}} = 0.10$). Node carrying capacities range from 400 (Howe Sound) to 1,000 (Sitka). This network reproduces three key empirical patterns: the north–south SSWD mortality gradient, fjord protection, and the absence of recovery in southern populations (Section 8).

6.5.2   11-Node Sensitivity Analysis Network

Sensitivity analysis Rounds 1–3 used a minimal 3-node network (Sitka, Howe Sound, Monterey) with inter-node distances of 1,700+ km—far exceeding the larval dispersal scale $D_L = 400\,\mathrm{km}$. Consequently, the spatial connectivity parameters (D_L, α_{self}) were effectively untestable, as the exponential kernel $\exp(-1700/400) < 10^{-2}$ produced negligible inter-node exchange regardless of D_L values within the SA range.

Round 4 introduced an 11-node stepping-stone chain with six additional intermediate nodes (Table 9), reducing maximum inter-node spacing to ∼452 km and ensuring that D_L values within the SA range [100, 1,000] km produce meaningful variation in larval exchange (32–76% at adjacent-node distances of 110–452 km with the default $D_L = 400\,\mathrm{km}$).

Table 9: 11-node stepping-stone network for sensitivity analysis Round 4. All nodes have $K = 5{,}000$ ($\sim$55,000 total agents). SST trend = $0.02\,^\circ\mathrm{C}\,\mathrm{yr}^{-1}$ for all nodes.

Node	Lat	Lon	$\bar{T}$ (°C)	A (°C)	S (psu)	ϕ (d^{-1})
Sitka	57.06	−135.34	8.0	3.5	32.0	0.80
Ketchikan	55.34	−131.64	8.5	3.5	31.0	0.50
Haida Gwaii	53.25	−132.07	9.0	3.0	31.5	0.60
Bella Bella	52.16	−128.15	9.5	3.5	28.0	0.40
Howe Sound*	49.52	−123.25	10.0	4.0	22.0	0.03
SJI	48.53	−123.02	10.5	4.0	30.0	0.30
Westport	46.89	−124.10	11.0	3.5	32.0	0.50
Newport	44.63	−124.05	11.5	3.0	33.0	0.60
Crescent City	41.76	−124.20	12.0	2.5	33.0	0.50
Fort Bragg	39.45	−123.80	12.5	2.5	33.5	0.50
Monterey	36.62	−121.90	13.0	2.5	33.5	0.40

*Fjord node (sill depth = 30 m, $\alpha_{\text{self}} = 0.30$). All other nodes open coast ($\alpha_{\text{self}} = 0.10$).

This upgrade substantially altered parameter importance rankings: $n_{\text{resistance}}$ rose from rank 19 to rank 5 (the three-trait partition amplifies genetic architecture importance at finer spatial scales), and $P_{\text{env,max}}$ rose from rank 11 to rank 4 (the environmental reservoir becomes critical with more nodes seeding independent epidemics). See Section **??** for full results.

6.5.3 Full-Range Network (Planned)

Scaling analysis (Section 8) demonstrated that the model supports 150-node networks at $\sim$66 s per 20-year run, enabling a full NE Pacific coastline simulation (Alaska to Baja California). This configuration will use the precomputed 489-site overwater distance matrix (Section 6.1.2) and site-specific SST forcing from satellite climatologies.

6.6 Network Construction

The `build_network` function assembles the metapopulation from a list of node definitions by: (i) computing the pairwise distance matrix (Haversine $\times\,\tau$ or precomputed overwater distances); (ii) constructing $\mathbf{C}$ with per-node α_j values (α_{fjord} or α_{open}), the D_L kernel, optional barrier factors, and row normalization to r_{total}; (iii) constructing $\mathbf{D}$ with the D_P kernel, flushing-rate modulation, sill attenuation, and the 50 km cutoff; and (iv) wrapping each node definition in a `SpatialNode` with initialized environmental state. The function accepts optional parameters for all kernel scales, self-recruitment fractions, and barrier configurations, allowing the same codebase to serve validation, sensitivity analysis, and full-range simulation.

7 Sensitivity Analysis

The SSWD-EvoEpi model contains 47 uncertain parameters spanning six modules: disease transmission and progression (16 parameters), genetics and trait architecture (8), population dynamics (7), spawning biology (7), pathogen virulence evolution (6), and spatial connectivity (3). Most of these parameters have limited empirical constraints (Section A), necessitating a systematic sensitivity analysis (SA) to identify which parameters most influence model behavior and, critically, which parameter *interactions* dominate the system's dynamics. We conducted a progressive, four-round SA campaign that tracked the model's growing complexity from a single-trait, 3-node prototype through to the full three-trait, 11-node eco-evolutionary framework.

7.1 Methods

7.1.1 Morris Elementary Effects Screening

Each SA round began with Morris elementary effects screening [48], implemented via the SALib Python library [26]. The Morris method is a one-at-a-time (OAT) design in which each parameter is perturbed along r independent trajectories through the p-dimensional input space. For parameter x_i in trajectory j, the elementary effect is

$$d_{ij} = \frac{f(x_1, \ldots, x_i + \Delta_i, \ldots, x_p) - f(x_1, \ldots, x_i, \ldots, x_p)}{\Delta_i}, \tag{69}$$

where Δ_i is the perturbation step. From these we compute two summary statistics per parameter per metric [8]:

- μ_i^*: the mean of the *absolute* elementary effects, measuring overall parameter importance regardless of sign;

- σ_i: the standard deviation of elementary effects, measuring interaction and nonlinearity strength.

When $\sigma_i/\mu_i^* > 1$, the parameter's influence on the metric is dominated by interactions with other parameters rather than by its direct (additive) effect [53]. To enable cross-metric comparison, we normalize μ^* by the range of the metric across all trajectories, then rank parameters by the mean normalized μ^* across all output metrics.

All rounds used $r = 20$ trajectories, yielding $r \times (p + 1)$ total model evaluations per round (e.g., $20 \times 48 = 960$ runs for the 47-parameter Round 4).

7.1.2 Sobol Variance Decomposition

Parameters surviving Morris screening advance to Sobol variance-based global sensitivity analysis [58], which decomposes the total output variance into contributions from individ-

ual parameters and their interactions. Using the Saltelli sampling scheme [52], $N(2p+2)$ model evaluations produce two key indices for each parameter x_i and output metric Y:

- $S_{1,i} = V_{x_i}[E_{x_{\sim i}}(Y|x_i)] \,/\, V(Y)$: the *first-order* Sobol index, measuring the fraction of output variance attributable to x_i alone;

- $S_{T,i} = 1 - V_{x_{\sim i}}[E_{x_i}(Y|x_{\sim i})] \,/\, V(Y)$: the *total-order* index, capturing x_i's contribution including all interactions with other parameters.

The gap $S_{T,i} - S_{1,i}$ quantifies the strength of parameter interactions. When $S_{T,i} \gg S_{1,i}$, the parameter's influence is mediated primarily through joint effects with other parameters, implying that it cannot be calibrated independently.

7.1.3 Output Metrics

The SA tracks 23 output metrics capturing demographic, evolutionary, spatial, and pathogen outcomes over 20-year simulations:

- **Demographic:** population crash percentage, final population fraction, recovery (population returns to >50% of initial), extinction (metapopulation collapse), peak single-year mortality, time to population nadir, total disease deaths, disease death fraction;

- **Evolutionary (host):** mean and maximum resistance shift ($\Delta \bar{r}$), tolerance shift ($\Delta \bar{t}$), recovery-trait shift ($\Delta \bar{c}$), additive variance retention ($V_A^{\mathrm{post}}/V_A^{\mathrm{pre}}$), evolutionary rescue index (composite of survival and resistance gain), total recovery events, recovery rate;

- **Spatial:** number of extinct nodes, north–south mortality gradient, fjord protection effect;

- **Pathogen:** mean final virulence, virulence shift ($\Delta \bar{v}$);

- **Spawning:** spawning participation rate, mean recruitment rate.

7.2 Progressive Sensitivity Analysis Design

The SA was conducted in four rounds (Table 10), each corresponding to a major model extension. This progressive design allows us to track how parameter importance shifts as model complexity grows—a critical diagnostic for identifying emergent behaviors introduced by new modules.

Table 10: Summary of sensitivity analysis rounds. Each round incorporates all changes from prior rounds. "New" parameters are those added relative to the previous round.

Round	Params	Metrics	Nodes	Runs	Key Changes
R1 (Morris)	23	14	3	480	Baseline: single resistance trait
R2 (Sobol)	23	14	3	12,288	Sobol decomposition of R1 params
R3 (Morris)	43	20	3	880	+20 params: pathogen evo, spawning, continuous mortality, daily growth
R4 (Morris)	47	23	11	960	+4 params: three-trait genetics, 11-node stepping-stone network

Rounds 1–2 (Pre–Three-Trait Baseline). The initial SA (Rounds 1–2) examined 23 parameters across disease (13), population (7), genetics (1: n_{additive}), and spawning (2) modules using a 3-node spatial network (Sitka, Howe Sound, Monterey; $K = 5{,}000$ per node). The model at this stage tracked a single resistance trait with n_{additive} additive loci. Morris screening (480 runs) retained all 23 parameters for Sobol analysis (12,288 runs, $N = 256$).

The Sobol decomposition revealed that disease progression rate $\mu_{\text{I2D,ref}}$ ($I_2 \rightarrow$ Death) was the single most influential parameter (mean $S_T = 0.638$), followed by susceptibility_multiplier ($S_T = 0.540$) and a_{exposure} ($S_T = 0.473$). A critical methodological finding was that Morris and Sobol rankings *disagreed*: Morris identified `settler_survival` and ρ_{rec} as the top drivers of population outcomes, while Sobol elevated susceptibility_multiplier and $\mu_{\text{I2D,ref}}$. This discrepancy arises because Morris measures marginal effects from extreme-value perturbations, whereas Sobol captures variance-weighted contributions including interactions. This confirmed that Morris screening alone is insufficient for identifying calibration priorities in this model.

Round 3 (Expanded Model, 3-Node). Round 3 added 20 parameters from four newly implemented modules: pathogen virulence evolution (6 parameters: virulence–fitness tradeoff exponents, mutation rate, initial virulence), expanded spawning biology (4: male spontaneous spawning, readiness induction, female bout limits, peak width), and additional disease mechanics (immunosuppression duration, minimum susceptible age, $I_1 \rightarrow I_2$ progression rate) and genetics parameters (target_mean_r, Beta-distribution shape parameters for initial allele frequencies). The network remained at 3 nodes for comparability with R1–R2.

Morris screening (880 runs, 20 trajectories) revealed a dramatic reshuffling: ρ_{rec} (recovery rate) rose to #1 ($\mu^*_{\text{norm}} = 0.642$), displacing $\mu_{\text{I2D,ref}}$ from its R1–R2 dominance. This occurred because the transition from discrete-stage to continuous daily mortality diluted the $I_2 \rightarrow$ Death rate's marginal influence, while recovery rate's role was amplified by its interaction with the new pathogen evolution module (higher ρ_{rec} imposes stronger selection against virulent strains). All 43 parameters exceeded the 5% elimination thresh-

old; zero were pruned.

Round 4 (Full Model, 11-Node). Round 4 represents the complete SSWD-EvoEpi model with two additions: (1) the three-trait genetic architecture (resistance, tolerance, recovery; Section 4.1), contributing four new parameters (target_mean_c, target_mean_t, $\tau_{\max}$, $n_{\text{tolerance}}$); and (2) an 11-node stepping-stone network spanning the latitudinal range of *Pycnopodia helianthoides* habitat. The expanded spatial network was critical for resolving spatial parameters that were undetectable at 3 nodes. This round (960 runs, 48 cores on an Intel Xeon W-3365) provides the most comprehensive screening of the model to date.

7.3 Round 4 Morris Results

7.3.1 Global Parameter Ranking

Table 12 presents the complete Round 4 Morris ranking for all 47 parameters, sorted by mean normalized μ^* across 23 output metrics. Figure 1 shows the top 20 parameters color-coded by module.

The top-10 parameters span four of six modules:

1. ρ_{rec} (recovery rate; $\mu^*_{\text{norm}} = 0.889$) — the rate at which infected individuals clear pathogen remains the single most influential parameter, as in R3. Its semi-additive behavior ($\sigma/\mu^* = 1.46$, the lowest interaction ratio of any parameter) reflects its direct mechanistic role: daily clearance probability $p_{\text{rec}} = \rho_{\text{rec}} \times c_i$ scales linearly with this rate regardless of other parameter values.

2. k_{growth} (von Bertalanffy growth rate; $\mu^*_{\text{norm}} = 0.633$) — faster growth accelerates maturation and spawning eligibility, providing demographic compensation during epidemics. Rose from #5 (R3) to #2.

3. K_{half} (half-infective dose; $\mu^*_{\text{norm}} = 0.622$) — the Michaelis–Menten saturation parameter controlling infection probability. Rose from #8 to #3.

4. $P_{\text{env,max}}$ (environmental reservoir; $\mu^*_{\text{norm}} = 0.598$) — background waterborne *V. pectenicida* input, independent of host shedding. Rose dramatically from #11 to #4, reflecting its interaction with the 11-node spatial network where environmental pathogen load varies with latitude and temperature.

5. $n_{\text{resistance}}$ (number of resistance loci; $\mu^*_{\text{norm}} = 0.525$) — genetic architecture of resistance. The largest rank gain of any parameter: #19 → #5 ($\Delta = +14$). The three-trait partition (17 loci per trait vs. the former 51 total) amplifies the sensitivity to how many loci underlie each defense mechanism.

46

6. s_0 (settler survival; $\mu^*_{\text{norm}} = 0.509$) — Beverton–Holt baseline recruitment. Dropped modestly from #3 to #6.

7. $\sigma_{2,\text{eff}}$ (late-stage shedding rate; $\mu^*_{\text{norm}} = 0.431$).

8. $\mu_{\text{I2D,ref}}$ ($I_2 \to$ Death rate; $\mu^*_{\text{norm}} = 0.419$) — formerly the #1 parameter in R1–R2 Sobol ($S_T = 0.638$), now #8 in R4 Morris.

9. σ_{spawn} (spawning peak width; $\mu^*_{\text{norm}} = 0.392$) — controls synchrony of the reproductive pulse; dropped from #2 to #9.

10. target_mean_c (initial mean recovery trait; $\mu^*_{\text{norm}} = 0.385$) — a *new* R4 parameter entering directly at #10, confirming that the recovery trait (c_i) is the fastest-evolving defense in the model (Section 4.1).
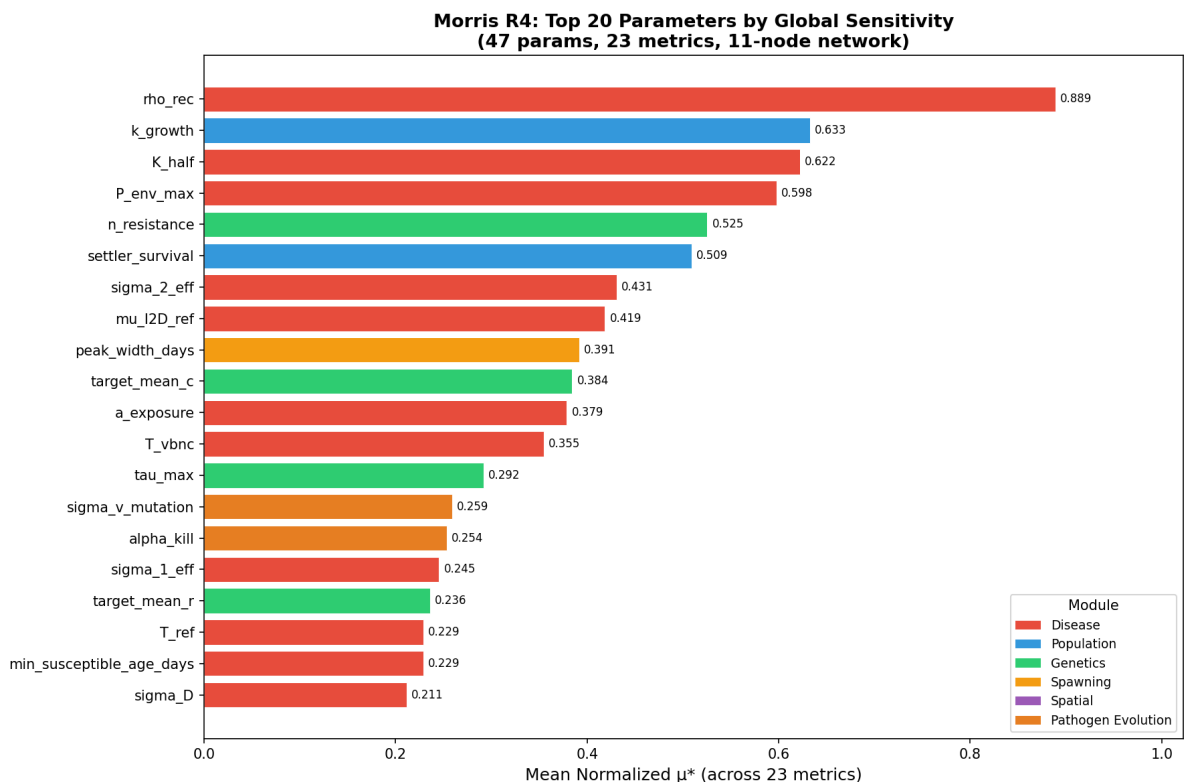
Figure 1: Top 20 parameters by mean normalized μ^* in Round 4 Morris screening (47 parameters, 23 metrics, 11-node network, 960 runs). Bars are color-coded by module. Error bars show 95% bootstrap confidence intervals across 20 trajectories.

7.3.2 Key Rank Shifts from Round 3

The transition from R3 to R4 produced dramatic rank changes (Figure 2), driven by two structural changes: the three-trait genetic architecture and the 11-node spatial network.

Major rank gains. Six parameters gained ≥ 7 ranks (Table 11):

- $\sigma_{1,\text{eff}}$ (early shedding rate): $\#43 \to \#16$ ($\Delta = +27$). Early shedding now interacts with pathogen evolution: σ_1 shapes the initial epidemic wave that determines the selection regime on virulence.

- $\sigma_{v,\text{mut}}$ (virulence mutation step size): $\#31 \to \#14$ ($\Delta = +17$). With 11 nodes providing diverse thermal and demographic environments, mutation rate controls how fast pathogen lineages adapt to local conditions.

- T_{ref} (pathogen temperature optimum): $\#34 \to \#18$ ($\Delta = +16$). The latitudinal temperature gradient across 11 nodes (vs. 3) amplifies the importance of the thermal reference point.

- $n_{\text{resistance}}$: $\#19 \to \#5$ ($\Delta = +14$), as discussed above.

- $\alpha_{\text{self,open}}$ (open-coast larval retention): $\#39 \to \#25$ ($\Delta = +14$). Spatial retention was invisible at 3 nodes but becomes detectable with 11 nodes and realistic dispersal distances.

- $P_{\text{env,max}}$: $\#11 \to \#4$ ($\Delta = +7$).

Major rank drops. Five parameters dropped ≥ 19 ranks:

- q_{init,β_b} (Beta-distribution shape b): $\#17 \to \#46$ ($\Delta = -29$). Initial allele-frequency shape is overwhelmed by the trait-specific mean parameters (target_mean_r/t/c).

- F_0 (reference fecundity): $\#20 \to \#47$ ($\Delta = -27$). Diluted in the expanded 47-parameter space.

- Immunosuppression duration: $\#15 \to \#42$ ($\Delta = -27$). Its effect is absorbed by spawning parameters and the recovery trait (c_i), which provides an alternative pathway through immunosuppressed periods.

- susceptibility_multiplier: $\#23 \to \#44$ ($\Delta = -21$). This parameter was $\#1$ in the R1–R2 Sobol analysis ($S_T = 0.540$); its precipitous decline reflects absorption by the explicit resistance genetics—individual r_i now captures susceptibility variation mechanistically, rendering the multiplicative modifier redundant.

- $p_{\text{spont,}}$ (female spontaneous spawning): $\#26 \to \#45$ ($\Delta = -19$).
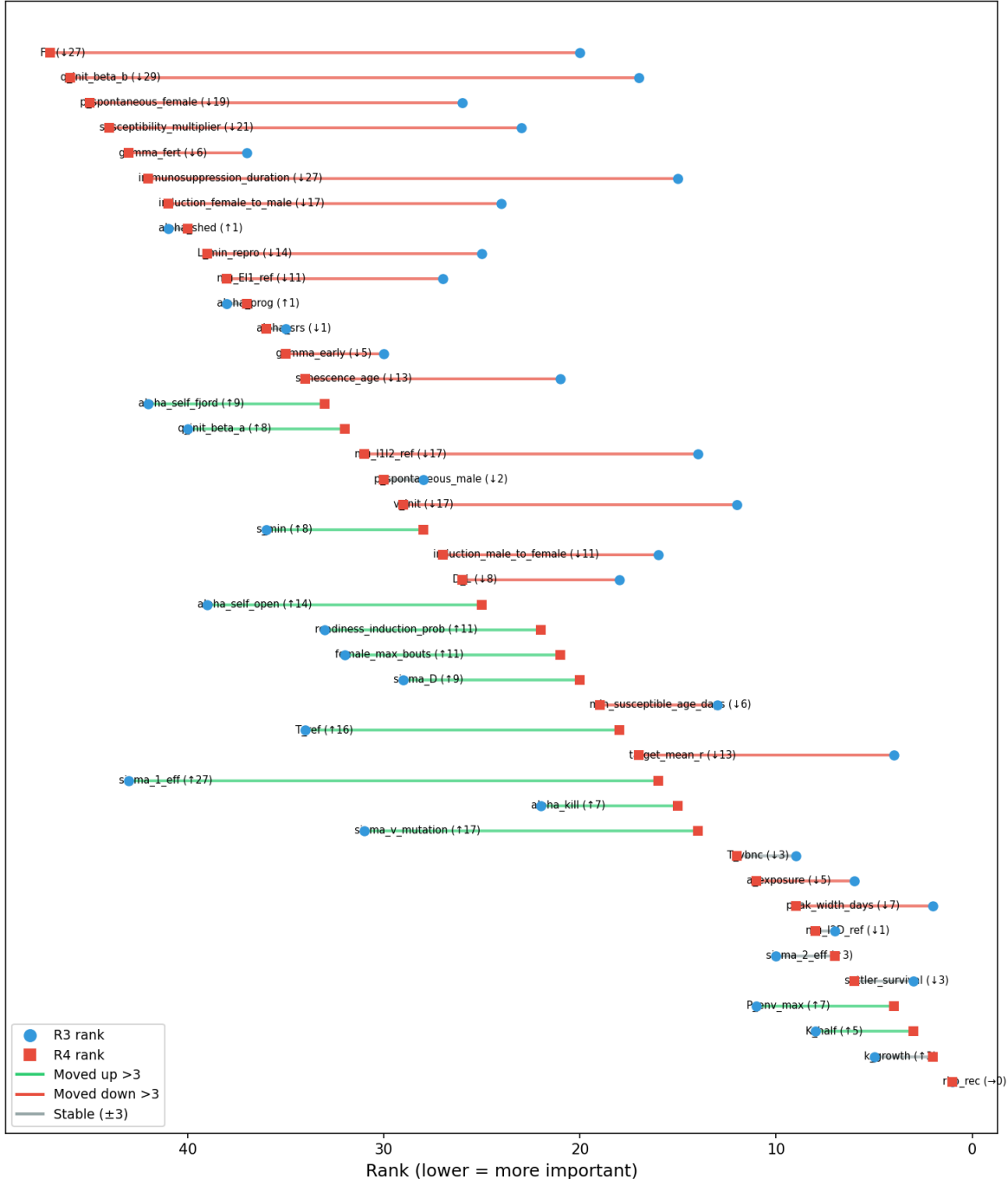
Figure 2: Rank change from Round 3 to Round 4 for the 43 parameters common to both rounds. Positive values (rightward) indicate increased importance in R4; negative values (leftward) indicate decreased importance. Parameters are sorted by R4 rank. Four new R4 parameters (not shown) entered at ranks #10, #13, #23, and #24.

Table 11: Largest rank shifts from R3 to R4 Morris screening. Positive Δ indicates increased importance.

Parameter	Module	R3 → R4	Δ	Mechanism
$\sigma_{1,\text{eff}}$	Disease	43 → 16	+27	Interacts with pathogen evolution
$\sigma_{v,\text{mut}}$	Pathogen evo.	31 → 14	+17	Controls adaptation speed
T_{ref}	Disease	34 → 18	+16	11-node thermal gradient
$n_{\text{resistance}}$	Genetics	19 → 5	+14	Three-trait partition
$\alpha_{\text{self,open}}$	Spatial	39 → 25	+14	Resolvable at 11 nodes
q_{init,β_b}	Genetics	17 → 46	−29	Absorbed by trait means
F_0	Population	20 → 47	−27	Diluted in larger space
Immunosupp. duration	Disease	15 → 42	−27	Absorbed by recovery trait
Suscept. multiplier	Disease	23 → 44	−21	Absorbed by resistance genetics

7.3.3   New Three-Trait Parameters

The four parameters introduced with the three-trait architecture (Section 4.1) immediately demonstrated meaningful sensitivity:

- target_mean_c (initial mean recovery trait): rank #10 ($\mu^*_{\text{norm}} = 0.385$). A top-10 entry confirms that recovery (c_i) is the dominant evolutionary pathway in the model, consistent with the validation finding that $\Delta\bar{c}$ exceeds $\Delta\bar{r}$ by $\sim 7\times$ at all nodes (Section 8).

- $\tau_{\max}$ (maximum tolerance scaling): rank #13 ($\mu^*_{\text{norm}} = 0.292$). The ceiling on how much tolerance extends I_2 survival matters because it sets the upper bound on the tolerance–recovery interaction.

- target_mean_t (initial mean tolerance): rank #23 ($\mu^*_{\text{norm}} = 0.197$). Mid-pack, reflecting the weaker selection signal on tolerance compared to recovery.

- $n_{\text{tolerance}}$ (number of tolerance loci): rank #24 ($\mu^*_{\text{norm}} = 0.189$). Mid-pack, but notably the most interacting parameter in the entire model ($\sigma/\mu^* = 2.51$), suggesting tolerance's role is context-dependent.

7.3.4   Universal Nonlinearity

A striking finding of the R4 Morris analysis is that *every one of the 47 parameters* has $\sigma/\mu^* > 1.0$ (Figure 3). This means that no parameter in the model acts additively—every parameter's effect on every metric depends on the values of other parameters. The model is a deeply coupled, nonlinear system.

The interaction ratio σ/μ^* ranges from 1.42 (s_0, settler survival) to 2.52 ($\sigma_{v,\text{mut}}$, virulence mutation rate). Two interaction tiers are apparent:

- **Moderately interacting** ($\sigma/\mu^* < 1.5$; 2 parameters): ρ_{rec} (1.46) and s_0 (1.42). These parameters operate semi-additively—their effects are relatively stable across parameter space. For ρ_{rec}, this reflects its direct mechanistic role: daily clearance probability scales linearly with recovery rate regardless of context.

- **Strongly to extremely interacting** ($\sigma/\mu^* > 1.5$; 45 parameters): the remaining parameters exhibit moderate to extreme nonlinearity. The most interacting parameters are genetic/evolutionary: $\sigma_{v,\text{mut}}$ (2.52), $n_{\text{tolerance}}$ (2.51), q_{init,β_a} (2.45), and α_{SRS} (2.34). These control *adaptation rates* that feed back on disease dynamics, which feed back on selection pressures—creating cascading interaction loops.

This universal nonlinearity has profound implications for calibration: no parameter can be tuned independently. Joint calibration via approximate Bayesian computation (ABC) or Markov chain Monte Carlo methods is essential.
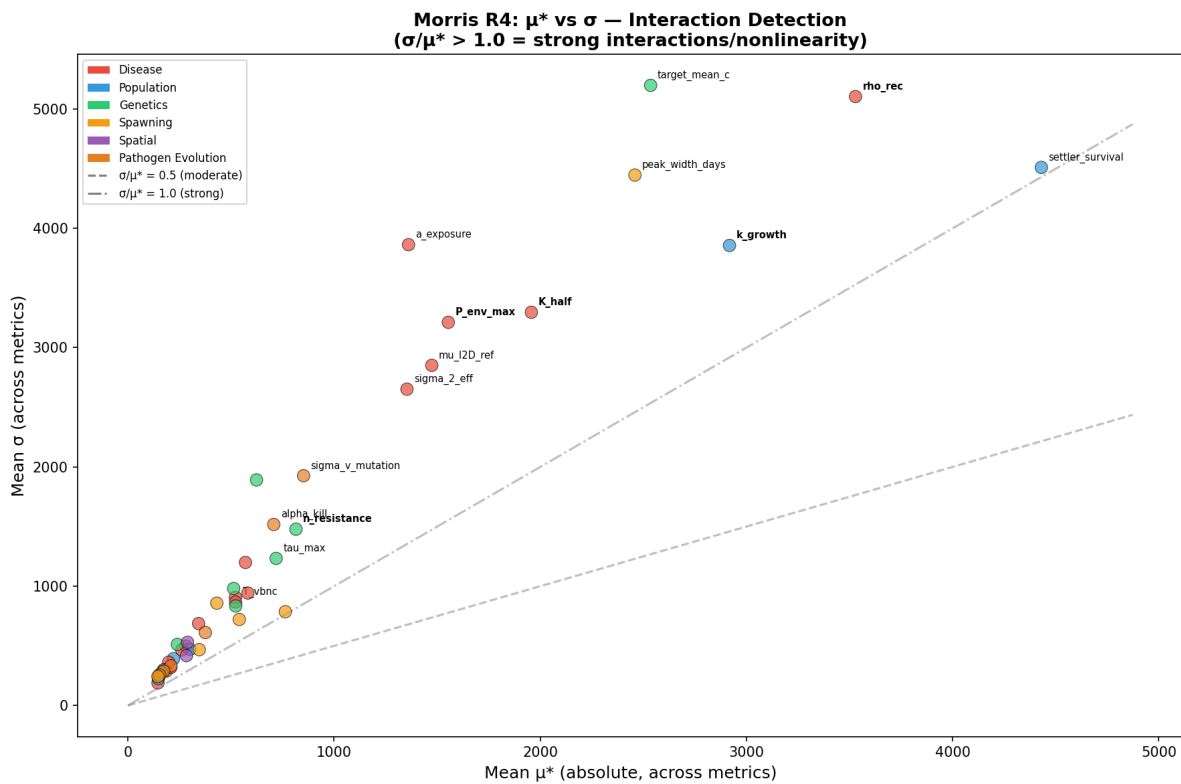
Figure 3: Morris μ^* vs. σ scatter for all 47 parameters (R4). The dashed line shows $\sigma = \mu^*$ (unit interaction ratio). All parameters fall above this line, indicating universal nonlinearity. Symbol color indicates module; symbol size scales with mean normalized μ^*.

7.3.5 Module-Level Sensitivity

Figure 4 summarizes sensitivity by module. The disease module dominates in both parameter count (16) and mean importance ($\overline{\mu^*_{\text{norm}}} = 0.332$), but genetics punches above

its weight: with only 8 parameters, it achieves the second-highest mean importance $(\overline{\mu^*_{\text{norm}}} = 0.260)$, and its top parameter ($n_{\text{resistance}}$) ranks #5 globally. The pathogen evolution module, despite being entirely new in R3–R4, achieves a mean $\mu^*_{\text{norm}} = 0.185$ with $\sigma_{v,\text{mut}}$ at #14—virulence evolution is not negligible and must be retained in calibration.

Spatial parameters $(\overline{\mu^*_{\text{norm}}} = 0.171)$ are detectable for the first time at 11 nodes. At the 3-node configuration of R1–R3, these parameters ranked #39–#42; at 11 nodes, they rise to #25–#33. This confirms that adequate spatial resolution is necessary to capture dispersal and retention dynamics.
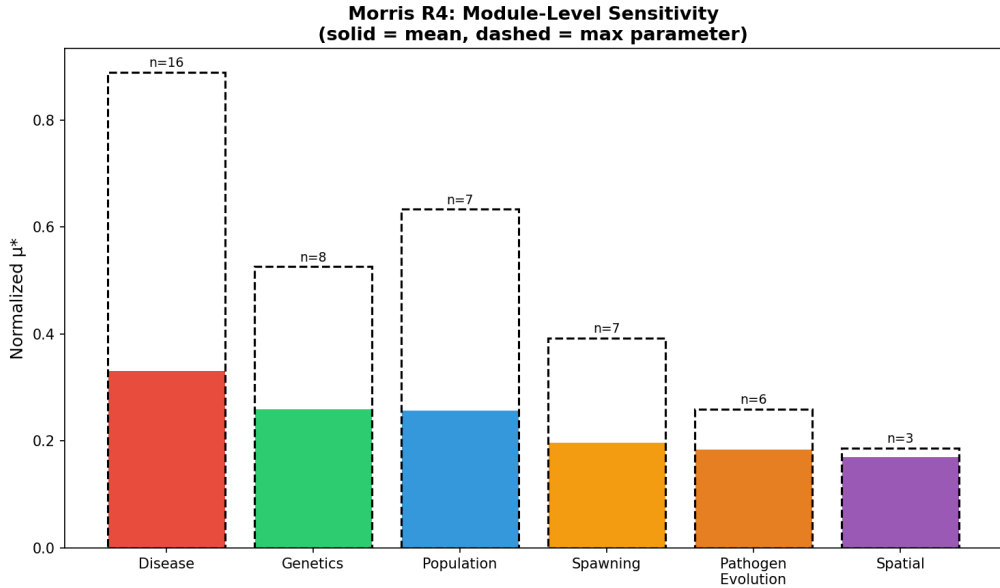

Figure 4: Module-level sensitivity summary for R4 Morris screening. Bar height shows mean normalized μ^* for each module; whiskers show the range from minimum to maximum parameter within each module. Number of parameters per module shown in parentheses.

7.4 Cross-Round Parameter Trajectories

Tracking individual parameters across all four rounds reveals which parameters have stable importance versus those whose influence is contingent on model structure (Figure 5):

Consistently important. ρ_{rec}, a_{exposure}, and $\sigma_{2,\text{eff}}$ remain in the top 12 across all rounds. These are robust calibration targets regardless of model configuration.

Structurally contingent. $\mu_{\text{I2D,ref}}$ was #1 in R1–R2 Sobol but dropped to #7–#8 in R3–R4 Morris after the switch to continuous daily mortality. susceptibility_multiplier fell from #1–#2 (R1–R2) to #44 (R4) as explicit resistance genetics absorbed its role. These shifts demonstrate that parameter importance can be an *artifact of model structure*,

not a property of the underlying biology, underscoring the need for structural sensitivity analysis alongside parametric SA.

Emergent with complexity. $P_{\text{env,max}}$, $n_{\text{resistance}}$, and all pathogen evolution parameters only revealed their importance at ≥ 11 nodes or ≥ 43 parameters. Simple model configurations systematically underestimate the importance of spatial and evolutionary parameters.
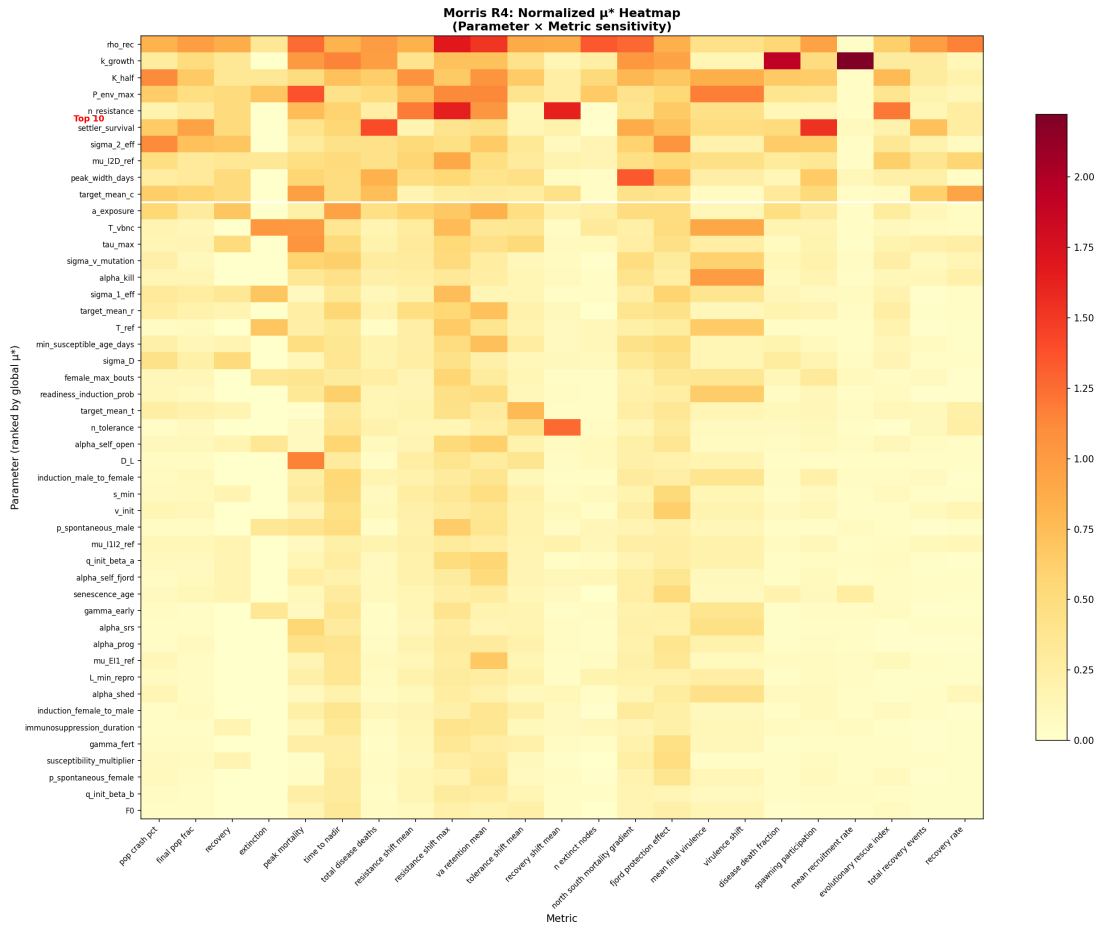
Figure 5: Parameter–metric sensitivity heatmap (R4 Morris). Cell color indicates normalized μ^* for each parameter–metric pair. Parameters (rows) are sorted by global rank; metrics (columns) are grouped by category. White cells indicate $\mu^*_{\text{norm}} < 0.05$.

7.5 Sobol Variance Decomposition: Rounds 1–2 and Ongoing

7.5.1 R1–R2 Sobol Results

The Round 1–2 Sobol analysis (23 parameters, $N = 256$, 12,288 runs) revealed massive parameter interactions across the model. For most metrics, total-order indices S_T far exceeded first-order indices S_1, meaning that parameter combinations dominate behavior over individual effects. Notable interaction signatures include:

- **Extinction:** $\sigma_{2,\text{eff}}$ had $S_T = 1.51$ but $S_1 \approx 0$—extinction risk is *entirely* driven by interactions between shedding rate and other parameters.

- **Fjord protection:** a_{exposure} had $S_T = 0.96$ but $S_1 = -0.12$—a negative first-order index means the parameter's effect *reverses sign* depending on the values of other parameters.

- **Recovery:** susceptibility_multiplier had $S_T = 0.96$ but $S_1 = 0.38$—60% of its influence arises through interactions.

7.5.2   Round 4 Sobol (In Progress)

A Round 4 Sobol analysis is currently running on a 48-core Intel Xeon W-3365 server. With 47 parameters and $N = 512$, the Saltelli design requires $N(2p + 2) = 49{,}152$ model evaluations at ~25 s each. At 12 parallel workers, the estimated wall time is approximately 7 days. This analysis will provide the first variance decomposition of the full three-trait, 11-node model and will enable direct comparison with the R1–R2 Sobol indices to quantify how the three-trait architecture redistributes variance among parameters.

Based on the R4 Morris results, we prioritize convergence monitoring for the top-10 parameters and anticipate particularly informative second-order (S_2) indices for the following parameter pairs:

- $\rho_{\text{rec}} \times$ target_mean_c: recovery rate $\times$ recovery genetics (both affect pathogen clearance);

- $P_{\text{env,max}} \times a_{\text{exposure}}$: environmental reservoir $\times$ transmission rate (dual exposure pathways);

- $n_{\text{resistance}} \times \sigma_{v,\text{mut}}$: host genetic architecture $\times$ pathogen adaptation rate (coevolutionary arms race);

- $k_{\text{growth}} \times s_0$: growth rate $\times$ recruitment (demographic compensation).

7.6   Summary and Implications

The four-round sensitivity analysis yields five principal findings:

1. **Recovery dominates.** The base recovery rate ρ_{rec} is consistently the most influential parameter across rounds and model configurations, yet has zero empirical basis. Determining whether *Pycnopodia helianthoides* can clear *V. pectenicida* infections—and at what rate—is the single highest-priority empirical question for model calibration.

2. **Genetic architecture is a structural choice with major consequences.** The number of resistance loci ($n_{\text{resistance}}$) ranks #5 globally and cannot be calibrated from data without high-resolution GWAS. The three-trait partition amplifies this sensitivity: 17 loci per trait behave very differently from 51 loci in a single trait.

3. **Parameter importance is model-contingent.** susceptibility_multiplier fell from #1 (R1–R2 Sobol) to #44 (R4 Morris) as explicit genetics absorbed its role; $\mu_{\text{I2D,ref}}$ fell from #1 to #8 with continuous mortality. SA results from simpler model configurations cannot be extrapolated to the full model.

4. **Universal nonlinearity demands joint calibration.** All 47 parameters interact ($\sigma/\mu^* > 1.0$). No parameter can be tuned independently. Approximate Bayesian computation with sequential Monte Carlo sampling (ABC-SMC) is the appropriate calibration framework.

5. **Spatial resolution matters.** Spatial and environmental parameters only emerge as important at ≥ 11 nodes. The planned 150-node full-coastline simulation will likely reveal additional spatially contingent sensitivities.

Table 12: Complete Round 4 Morris parameter ranking (47 parameters, 23 metrics, 11-node network, 960 runs). Mean normalized μ^* is averaged across all metrics. The σ/μ^* ratio indicates interaction strength (> 1: interaction-dominated). R3 Rank column shows the parameter's position in the 43-parameter R3 analysis; "—" indicates a new R4 parameter.

Rank	Parameter	Module	$\overline{\mu^*_{\mathrm{norm}}}$	σ/μ^*	R3	Δ
1	ρ_{rec}	Disease	0.889	1.46	1	—
2	k_{growth}	Population	0.633	1.63	5	↑3
3	K_{half}	Disease	0.622	1.84	8	↑5
4	$P_{\mathrm{env,max}}$	Disease	0.598	1.92	11	↑7
5	$n_{\mathrm{resistance}}$	Genetics	0.525	1.78	19	↑14
6	s_0 (settler survival)	Population	0.509	1.42	3	↓3
7	$\sigma_{2,\mathrm{eff}}$	Disease	0.431	1.95	10	↑3
8	$\mu_{\mathrm{I2D,ref}}$	Disease	0.419	1.98	7	↓1
9	σ_{spawn} (peak width)	Spawning	0.392	2.03	2	↓7
10	target_mean_c	Genetics	0.385	2.08	—	—
11	a_{exposure}	Disease	0.379	2.20	6	↓5
12	T_{VBNC}	Disease	0.355	2.07	9	↓3
13	τ_{max}	Genetics	0.292	2.05	—	—
14	$\sigma_{v,\mathrm{mut}}$	Path. evo.	0.259	2.52	31	↑17
15	α_{kill}	Path. evo.	0.254	2.25	22	↑7
16	$\sigma_{1,\mathrm{eff}}$	Disease	0.245	2.24	43	↑27
17	target_mean_r	Genetics	0.236	1.86	4	↓13
18	T_{ref}	Disease	0.229	1.94	34	↑16
19	min. susceptible age	Disease	0.229	2.04	13	↓6

Table 12 (continued)

Rank	Parameter	Module	$\overline{\mu^*_{\text{norm}}}$	σ/μ^*	R3	Δ
20	σ_D	Disease	0.211	1.96	29	↑9
21	female max bouts	Spawning	0.206	1.95	32	↑11
22	readiness induction prob.	Spawning	0.204	2.26	33	↑11
23	target_mean_t	Genetics	0.197	2.05	—	—
24	$n_{\text{tolerance}}$	Genetics	0.189	2.51	—	—
25	$\alpha_{\text{self,open}}$	Spatial	0.187	2.07	39	↑14
26	D_L	Spatial	0.178	2.29	18	↓8
27	κ_{mf} (M→F induction)	Spawning	0.176	2.07	16	↓11
28	s_{min}	Disease	0.175	1.84	36	↑8
29	v_{init}	Path. evo.	0.173	2.13	12	↓17
30	$p_{\text{spont,m}}$	Spawning	0.169	2.11	28	↓2
31	$\mu_{\text{I1I2,ref}}$	Disease	0.156	1.97	14	↓17
32	q_{init,β_a}	Genetics	0.150	2.45	40	↑8
33	$\alpha_{\text{self,fjord}}$	Spatial	0.149	2.00	42	↑9
34	senescence age	Population	0.148	1.66	21	↓13
35	γ_{early}	Path. evo.	0.148	2.03	30	↓5
36	α_{SRS}	Population	0.146	2.34	35	↓1
37	α_{prog}	Path. evo.	0.143	2.09	38	↑1
38	$\mu_{\text{EI1,ref}}$	Disease	0.141	2.19	27	↓11
39	$L_{\text{min,repro}}$	Population	0.139	2.06	25	↓14
40	α_{shed}	Path. evo.	0.136	2.12	41	↑1

Table 12 (continued)

Rank	Parameter	Module	$\overline{\mu^*_{\text{norm}}}$	σ/μ^*	R3	Δ
41	κ_{fm} (F→M induction)	Spawning	0.130	1.79	24	↓17
42	immunosupp. duration	Disease	0.127	2.07	15	↓27
43	γ_{fert}	Population	0.122	2.21	37	↓6
44	suscept. multiplier	Disease	0.111	2.03	23	↓21
45	$p_{\text{spont,f}}$	Spawning	0.110	1.67	26	↓19
46	q_{init,β_b}	Genetics	0.104	2.20	17	↓29
47	F_0	Population	0.102	1.83	20	↓27

8 Validation

9 Discussion

References

[1] Emilius A. Aalto, Kevin D. Lafferty, Susanne H. Sokolow, Richard E. Grewelle, Tal Ben-Horin, Charles A. Boch, Peter T. Raimondi, Steven J. Bograd, Elliott L. Hazen, Michael G. Jacox, Fiorenza Micheli, and Giulio A. De Leo. Models with environmental drivers offer a plausible mechanism for the rapid spread of infectious disease outbreaks in marine organisms. *Scientific Reports*, 10:5975, 2020. doi: 10.1038/s41598-020-62118-4.

[2] Citlalli A. Aquino, Ryan M. Besemer, Christopher M. DeRito, Jan Kocian, Ian R. Porter, Peter T. Raiber, John E. Episale, and Ian Hewson. Evidence that microorganisms at the animal-water interface drive sea star wasting disease. *Frontiers in Microbiology*, 11:610009, 2021. doi: 10.3389/fmicb.2020.610009.

[3] Einar Árnason, Jere Koskela, Katrín Halldórsdóttir, and Bjarki Eldon. Sweepstakes reproductive success via pervasive and recurrent selective sweeps. *eLife*, 12:e80781, 2023. doi: 10.7554/eLife.80781.

[4] Jorge Arroyo-Esquivel, Alyssa Gehman, Katie Collins, and Fernanda Sanchez. Managing populations after a disease outbreak: exploration of epidemiological consequences of managed host reintroduction following disease-driven host decline. *bioRxiv*, 2025. doi: 10.1101/2025.02.28.640833.

[5] AZA SAFE. Sunflower sea star program plan 2024–2027. Technical report, Association of Zoos and Aquariums, 2024.

[6] Jenn M. Burt, M. Tim Tinker, Daniel K. Okamoto, Kyle W. Demes, Katie Holmes, and Anne K. Salomon. Sudden collapse of a mesopredator reveals its complementary role in mediating rocky reef regime shifts. *Proceedings of the Royal Society B*, 285: 20180553, 2018. doi: 10.1098/rspb.2018.0553.

[7] California Ocean Protection Council. Staff recommendation item 9: Consideration and approval of disbursement of funds to support sunflower sea star reintroduction. Technical report, California Ocean Protection Council, 2025.

[8] Francesca Campolongo, Jessica Cariboni, and Andrea Saltelli. An effective screening design for sensitivity analysis of large models. *Environmental Modelling & Software*, 22(10):1509–1518, 2007. doi: 10.1016/j.envsoft.2006.10.004.

[9] Matthew Clement, Rodrigo Hamede, Menna E. Jones, and Paul A. Hohenlohe. Coevolution enables host persistence in an eco-evolutionary epidemiological model of Tasmanian devil facial tumor disease. *Evolution*, 78(12):2095–2110, 2024. doi: 10.1093/evolut/qpae143.

[10] Matthew Clement et al. Eco-evolutionary individual-based model for coevolution between Tasmanian devils and devil facial tumour disease. *Evolution*, 2024. doi: 10.1093/evolut/qpae143.

[11] Donald L. DeAngelis and Wolf M. Mooij. Individual-based modeling of ecological and evolutionary processes. *Annual Review of Ecology, Evolution, and Systematics*, 36:147–168, 2005. doi: 10.1146/annurev.ecolsys.36.102003.152644.

[12] Michael L. Dungan, Thomas E. Miller, and Donald A. Thomson. Catastrophic decline of a top carnivore in the Gulf of California rocky intertidal zone. *Science*, 216:989–991, 1982. doi: 10.1126/science.216.4549.989.

[13] Morgan E. Eisenlord, Maya L. Groner, Robin M. Yoshioka, Jennifer Elliott, Jeffrey Maynard, Steven Fradkin, Margaret Turner, Katie Pyne, Sandy Wyllie-Echeverria, Benjamin G. Miner, and C. Drew Harvell. Ochre star mortality during the 2014 wasting disease epizootic: role of population size and temperature. *Philosophical Transactions of the Royal Society B*, 371(1689):20150212, 2016. doi: 10.1098/rstb. 2015.0212.

[14] Bjarki Eldon and Wolfgang Stephan. Sweepstakes reproduction facilitates rapid adaptation in highly fecund populations. *Molecular Ecology*, 33:e16903, 2024. doi: 10.1111/mec.16903.

[15] Aaron W. E. Galloway, Sarah A. Gravem, Jenna N. Kobelt, et al. Sunflower sea star predation on urchins can facilitate kelp forest recovery. *Proceedings of the Royal Society B*, 290:20221897, 2023. doi: 10.1098/rspb.2022.1897.

[16] Joanna C. Gascoigne and Romuald N. Lipcius. Allee effects in marine systems. *Marine Ecology Progress Series*, 269:49–59, 2004. doi: 10.3354/meps269049.

[17] Àlex Giménez-Romero, Antoni Grau, Iris E. Hendriks, and Manuel A. Matías. Modelling parasite-produced marine diseases: The case of the mass mortality event of *Pinna nobilis*. *Ecological Modelling*, 459:109740, 2021. doi: 10.1016/j.ecolmodel. 2021.109740.

[18] Sarah A. Gravem and Bruce A. Menge. Metapopulation-scale resilience to disease-induced mass mortality in a keystone predator: From stasis to instability. *Ecosphere*, 16:e70426, 2025. doi: 10.1002/ecs2.70426.

[19] Sarah A. Gravem, Walter N. Heady, Vienna R. Saccomanno, Kathleen F. Alvstad, Alyssa-Lois M. Gehman, Taylor N. Frierson, and Scott L. Hamilton. *Pycnopodia helianthoides. The IUCN Red List of Threatened Species*, 2021. doi: 10.2305/IUCN. UK.2021-1.RLTS.T178290276A197818455.en.

[20] Volker Grimm and Steven F. Railsback. *Individual-Based Modeling and Ecology.* Princeton University Press, Princeton, NJ, 2005.

[21] Mary Hagedorn et al. Assisted gene flow using cryopreserved sperm in critically endangered coral. *Proceedings of the National Academy of Sciences*, 118:e2110559118, 2021. doi: 10.1073/pnas.2110559118.

[22] Scott L. Hamilton et al. Disease-driven mass mortality event leads to widespread extirpation and variable recovery potential of a marine predator across the eastern Pacific. *Proceedings of the Royal Society B*, 288:20211195, 2021. doi: 10.1098/rspb. 2021.1195.

[23] C. Drew Harvell, Diego Montecino-Latorre, Joseph M. Caldwell, Jenn M. Burt, Kathryn Bosley, et al. Disease epidemic and a marine heat wave are associated with the continental-scale collapse of a pivotal predator (*Pycnopodia helianthoides*). *Science Advances*, 5:eaau7042, 2019. doi: 10.1126/sciadv.aau7042.

[24] Walter N. Heady, Rodrigo Beas-Luna, Michael N. Dawson, et al. Roadmap to recovery for the sunflower sea star along the West Coast of North America. Technical report, The Nature Conservancy, 2022.

[25] Dennis Hedgecock and Alexander I. Pudovkin. Sweepstakes reproductive success in highly fecund marine fish and shellfish: A review and commentary. *Bulletin of Marine Science*, 87:971–1002, 2011. doi: 10.5343/bms.2010.1051.

[26] Jon Herman and Will Usher. SALib: An open-source Python library for sensitivity analysis. *Journal of Open Source Software*, 2(9):97, 2017. doi: 10.21105/joss.00097.

[27] Ian Hewson. Microbial respiration in the asteroid diffusive boundary layer influenced sea star wasting disease during the 2013–2014 northeast Pacific Ocean mass mortality event. *Marine Ecology Progress Series*, 668:231–237, 2021. doi: 10.3354/meps13710.

[28] Ian Hewson. When bacteria meet many arms: Autecological insights into *Vibrio pectinicida* FHCF-3 in echinoderms. *bioRxiv*, 2025. doi: 10.1101/2025.08.15.670479.

[29] Ian Hewson, Jason B. Button, Brent M. Gudenkauf, et al. Densovirus associated with sea-star wasting disease and mass mortality. *Proceedings of the National Academy of Sciences*, 111:17278–17283, 2014. doi: 10.1073/pnas.1416625111.

[30] Ian Hewson, Morgan R. Johnson, and Benjamin Reyes-Chavez. Lessons learned from the sea star wasting disease investigation. *Annual Review of Marine Science*, 17:257–279, 2025. doi: 10.1146/annurev-marine-040623-082617.

[31] Ian Hewson et al. Investigating the complex association between viral ecology, environment, and Northeast Pacific sea star wasting. *Frontiers in Marine Science*, 5:77, 2018. doi: 10.3389/fmars.2018.00077.

[32] Ian Hewson et al. Perspective: Something old, something new? Review of wasting and other mortality in Asteroidea (Echinodermata). *Frontiers in Marine Science*, 6: 406, 2019. doi: 10.3389/fmars.2019.00406.

[33] Jason Hodin, Amanda Pearson-Lund, Freya P. Anteau, Philippe Kitaeff, and Sarah Cefalu. Progress toward complete life-cycle culturing of the endangered sunflower star, *Pycnopodia helianthoides. Biological Bulletin*, 241:243–258, 2021. doi: 10.1086/716552.

[34] Ilse Höllinger, Pleuni S. Pennings, and Joachim Hermisson. Polygenic adaptation: From sweeps to subtle frequency shifts. *eLife*, 11:e66697, 2022. doi: 10.7554/eLife.66697.

[35] C. Lambert, J.-L. Nicolas, V. Cilia, and S. Corre. Vibrio pectenicida sp. nov., a pathogen of scallop (Pecten maximus) larvae. *International Journal of Systematic Bacteriology*, 48:481–487, 1998. doi: 10.1099/00207713-48-2-481.

[36] Ryan E. Langendorf, James A. Estes, James C. Watson, Michael C. Kenner, Brian B. Hatfield, M. Tim Tinker, Elizabeth Waddle, Michelle L. DeMarch, and Daniel F. Doak. Dynamic and context-dependent keystone species effects in kelp forests. *Proceedings of the National Academy of Sciences*, 2025. doi: 10.1073/pnas.XXXXXXX.

[37] Harilaos A. Lessios. The great *Diadema antillarum* die-off: 30 years later. *Annual Review of Marine Science*, 8:267–283, 2016. doi: 10.1146/annurev-marine-122414-033857.

[38] Katie E. Lotterhos and Michael C. Whitlock. The relative power of genome scans to detect local adaptation depends on sampling design and statistical method. *Molecular Ecology*, 24(5):1031–1046, 2015. doi: 10.1111/mec.13100.

[39] Dayv Lowry, Sarah Wright, Melissa Neuman, et al. Endangered Species Act status review report: Sunflower sea star (*Pycnopodia helianthoides*). Technical report, NOAA National Marine Fisheries Service, 2022.

[40] Carolyn J. Lundquist and Louis W. Botsford. Model projections of the fishery implications of the Allee effect in broadcast spawners. *Ecological Applications*, 14: 929–941, 2004. doi: 10.1890/02-5325.

[41] Coralie Lupo, Pedro J. Cabello-Yeves, Sara Ferreira, Julien de Lorgeril, and Luigi Vezzulli. Vibrio ecology, pathogenesis, and evolution. *Frontiers in Microbiology*, 11: 587685, 2020. doi: 10.3389/fmicb.2020.587685.

[42] Coralie Lupo et al. Spatial epidemiological modelling of infection by *Vibrio aestuarianus* shows that connectivity and temperature control oyster mortality. *Aquaculture Environment Interactions*, 12:511–527, 2020. doi: 10.3354/aei00379.

[43] Michael Lynch. Evolution of the mutation rate. *Trends in Genetics*, 26:345–352, 2010. doi: 10.1016/j.tig.2010.05.003.

[44] Ryan T. Mancuso, Sarah A. Gravem, Rachel S. Campbell, Nathan Hunter, Pete Raimondi, Aaron W. E. Galloway, and Kristy J. Kroeker. Sunflower sea star chemical cues locally reduce kelp consumption by eliciting a flee response in red sea urchins. *Proceedings of the Royal Society B*, 2025. doi: 10.1098/rspb.2025.0949.

[45] Zofia D. Meunier, Sally D. Hacker, and Bruce A. Menge. Regime shifts in rocky intertidal communities associated with a marine heatwave and disease outbreak. *Nature Ecology & Evolution*, 8:1285–1297, 2024. doi: 10.1038/s41559-024-02425-5.

[46] C. Melissa Miner, Jennifer L. Burnaford, Richard F. Ambrose, Liam Antrim, et al. Large-scale impacts of sea star wasting disease (SSWD) on intertidal sea stars and implications for recovery. *PLoS ONE*, 13:e0192870, 2018. doi: 10.1371/journal.pone.0192870.

[47] Diego Montecino-Latorre, Morgan E. Eisenlord, Morgan Turner, Reyn Yoshioka, C. Drew Harvell, et al. Devastating transboundary impacts of sea star wasting disease on subtidal asteroids. *PLoS ONE*, 11:e0163190, 2016. doi: 10.1371/journal.pone.0163190.

[48] Max D. Morris. Factorial sampling plans for preliminary computational experiments. *Technometrics*, 33(2):161–174, 1991. doi: 10.1080/00401706.1991.10484804.

[49] Maya B. Prentice, Citlalli A. Aquino, Amy M. Chan, Kalia M. Davis, Paul K. Hershberger, Jan F. Finke, Jason Hodin, Aquiala McCracken, Christina T. E. Kellogg, Rute B. G. Clemente-Carvalho, Christy Prentice, Kiana X. Zhong, C. Drew Harvell, Curtis A. Suttle, and Alyssa-Lois M. Gehman. *Vibrio pectenicida* strain FHCF-3 is a causative agent of sea star wasting disease. *Nature Ecology & Evolution*, 2025. doi: 10.1038/s41559-025-02797-2.

[50] Lars Råberg, Andrea L. Graham, and Andrew F. Read. Decomposing health: toler- ance and resistance to parasites in animals. *Philosophical Transactions of the Royal Society B*, 364(1513):37–49, 2009. doi: 10.1098/rstb.2008.0184.

[51] Laura Rogers-Bennett and Cynthia A. Catton. Marine heat wave and multiple stressors tip bull kelp forest to sea urchin barrens. *Scientific Reports*, 9:15050, 2019. doi: 10.1038/s41598-019-51114-y.

[52] Andrea Saltelli. Making best use of model evaluations to compute sensitivity in- dices. *Computer Physics Communications*, 145(2):280–297, 2002. doi: 10.1016/ S0010-4655(02)00280-1.

[53] Andrea Saltelli, Marco Ratto, Terry Andres, Francesca Campolongo, Jessica Cari- boni, Debora Gatelli, Michaela Saisana, and Stefano Tarantola. *Global Sensitivity Analysis: The Primer*. John Wiley & Sons, 2008. doi: 10.1002/9780470725184.

[54] Lauren M. Schiebelhut, Jonathan B. Puritz, and Michael N. Dawson. Decimation by sea star wasting disease and rapid genetic change in a keystone species, *Pisaster ochraceus*. *Proceedings of the National Academy of Sciences*, 115:7069–7074, 2018. doi: 10.1073/pnas.1800285115.

[55] Lauren M. Schiebelhut, Jonathan B. Puritz, and Michael N. Dawson. Decimation by sea star wasting disease and rapid genetic change in a keystone species, *Pisaster ochraceus*. *Proceedings of the National Academy of Sciences*, 115(27):7069–7074, 2018. doi: 10.1073/pnas.1800285115.

[56] Lauren M. Schiebelhut et al. A reference genome for ecological restoration of the sunflower sea star, *Pycnopodia helianthoides*. *Journal of Heredity*, 115:86–93, 2024. doi: 10.1093/jhered/esad054.

[57] Sea Star Lab. Sea star cryopreservation breakthrough inspires hope for sunflower stars, 2025. Press release.

[58] Il'ya M. Sobol'. Global sensitivity indices for nonlinear mathematical models and their Monte Carlo estimates. *Mathematics and Computers in Simulation*, 55(1–3): 271–280, 2001. doi: 10.1016/S0378-4754(00)00270-6.

[59] Sunflower Star Lab. First-ever temporary experimental outplanting of sunflower stars in California, 2025. Press release.

[60] Nick Tolimieri. Appendix A: Population viability analysis of *Pycnopodia he- lianthoides. In: Lowry et al., ESA Status Review Report, NOAA NMFS*, 2022.

[61] David L. J. Vendrami, Lloyd S. Peck, Melody S. Clark, Bjarki Eldon, Michael Meredith, and Joseph I. Hoffman. Sweepstake reproductive success and collective dispersal produce chaotic genetic patchiness in a broadcast spawner. *Science Advances*, 7: eabj4713, 2021. doi: 10.1126/sciadv.abj4713.

[62] John P. Wares and Lauren M. Schiebelhut. What doesn't kill them makes them stronger: an association between elongation factor 1-α overdominance in the sea star *Pisaster ochraceus* and "sea star wasting disease". *PeerJ*, 4:e1876, 2016. doi: 10.7717/peerj.1876.

[63] Helen J. Wearing, Pejman Rohani, and Matt J. Keeling. Appropriate models for the management of infectious diseases. *PLoS Medicine*, 2(7):e174, 2005. doi: 10.1371/journal.pmed.0020174.

A   Parameter Tables